inorganics

MDPI

Article

Synthesis of Some Novel Cr(III), Mn(II), and Pd(II) Complexes via the Sono-Chemical Route with a Chlorinated Quinolinyl-Imine Ligand: Structural Elucidation, Bioactivity Analysis, and Docking Simulations

Dalal Alhashmialameer

Chemistry Department, College of Science, Taif University, Taif 21944, Saudi Arabia; dsamer@tu.edu.sa

Abstract

The present study reports the sono-chemical synthesis of novel nanosized Cr(III), Mn(II), and Pd(II) complexes incorporating the chloro-2-(quinolin-8-yliminomethyl)-phenol imine ligand. The synthesized complexes were characterized using various spectroscopic and analytical techniques, including Fourier-transform infrared (FT-IR) spectroscopy, ultraviolet–visible (UV–Vis) spectroscopy, scanning electron microscopy (SEM), and thermal gravimetric analysis (TGA). The results confirmed the successful coordination of the ligand-to-metal centers, forming stable nanosized metal complexes with distinct physicochemical properties. Biological evaluations, including antimicrobial and antioxidant assays, revealed that the synthesized complexes exhibited enhanced biological activity compared to the free ligand, demonstrating potent antibacterial and antifungal properties against various pathogenic strains. The potential of the complexes to serve as efficient free-radical inhibitors was determined by employing DPPH radical scavenging assays, which underscored their significant antioxidant properties. Furthermore, molecular docking studies were conducted to elucidate the binding interactions of the metal complexes with biological targets, providing insights into their mechanism of action. The findings suggest that the synthesized nanosized Cr(III), Mn(II), and Pd(II) complexes possess promising biological properties, making them potential candidates for pharmaceutical and biomedical applications. The study also demonstrates the effectiveness of sono-chemical synthesis in producing nanosized metal complexes with enhanced physicochemical and biological characteristics.

Keywords: sono-chemical synthesis; nanosized metal complexes; quinolinyl-imine ligand; Cr(III); Mn(II); Pd(II); biological activity; molecular docking

check for updates

Academic Editors: Wolfgang Linert and Vinay K. Sharma

Received: 25 June 2025
Revised: 8 August 2025
Accepted: 13 August 2025
Published: 18 August 2025

Citation: Alhashmialameer, D. Synthesis of Some Novel Cr(III), Mn(II), and Pd(II) Complexes via the Sono-Chemical Route with a Chlorinated Quinolinyl-Imine Ligand: Structural Elucidation, Bioactivity Analysis, and Docking Simulations. *Inorganics* **2025**, *13*, 271. https://doi.org/10.3390/inorganics13080271

Correction Statement: This article has been republished with a minor change. The change does not affect the scientific content of the article and further details are available within the backmatter of the website version of this article.

Copyright: © 2025 by the author. Licensee MDPI, Basel, Switzerland. This article is an open access article distributed under the terms and conditions of the Creative Commons Attribution (CC BY) license (https://creativecommons.org/licenses/by/4.0/).

1. Introduction

Pharmaceutical innovation frequently involves a chemical strategy that combines several molecules to produce new ones with unprecedented biological properties. The synthesis of compounds, particularly the versatile class of Schiff bases, is notable for their anticancer, antibacterial, and anti-inflammatory characteristics, as well as various catalytic, optical, and sensing properties [1–4]. These molecules readily interact with almost every metal ion, which is why they are pivotal components in the realm of coordination chemistry. The objective of creating metal complexes is to tailor their physicochemical properties due to the broad spectrum of coordination environments, oxidation states, redox potentials, and ligand arrangements. Consequently, the biological actions of diverse ligands are significantly influenced when they form complexes [5–7]. The domain of metal-complex-based

anticancer therapy is in a constant state of advancement, with scientists investigating innovative metal complexes, combination treatments, targeted delivery mechanisms, and tactics to surmount resistance [8–10]. Personalized medical approaches, which consider the individual genetic profiles of patients and their tumor cells, show substantial promise for enhancing the effectiveness of these therapies and reducing side effects. This category of metal-based treatments represents a vast and promising avenue for cancer care, potentially leading to superior outcomes. Furthermore, antimicrobial metal complexes boast a multitude of potential uses across different sectors, including medical applications such as antimicrobial medications and wound coverings, agricultural purposes like pesticides and fungicides, and consumer goods like antimicrobial coatings for various surfaces. A significant hurdle in the development of these complexes lies in achieving selective toxicity towards pathogenic microbes while minimizing harm to human cells. The design focus is on complexes that can target microbial cells with precision, thereby reducing the impact on the host organism. This selectivity is essential for their successful application across various fields. The design and synthesis of transition metal complexes with Schiff base ligands have attracted significant interest due to their diverse structural features, chemical versatility, and broad spectrum of biological applications, including antimicrobial, anticancer, and antioxidant activities [11,12]. Schiff bases, derived from the condensation of primary amines with carbonyl compounds, possess azomethine (-C=N-) functional groups, which facilitate strong coordination with metal ions, thereby enhancing their stability and biological properties [13]. Among the various Schiff base ligands, those incorporating quinoline moieties have demonstrated remarkable pharmacological potential due to their π-conjugated system, which enhances electronic interactions and biological activity [14]. The incorporation of metal ions such as chromium Cr(III), manganese Mn(II), and palladium Pd (II) into these ligands is particularly interesting, as these metals exhibit diverse coordination geometries and oxidation states, influencing the electronic and biological behavior of the resulting complexes [15,16]. Ultrasound-assisted (sono-chemical) synthesis has emerged as a promising technique in the preparation of nanostructured metal complexes, offering advantages such as improved reaction rates, reduced particle size, and enhanced purity compared to conventional synthetic routes [17]. Sono-chemical methods induce cavitation effects, leading to localized high temperatures and pressures, which significantly impact nucleation and growth kinetics, favoring the formation of nanosized materials with improved physicochemical properties [18].

The investigated ligand, chloro-2-(quinolin-8-yliminomethyl)-phenol, was not chosen arbitrarily. It features a Schiff base framework renowned for its versatility in coordination chemistry, yet distinguished by a unique combination of functional groups that enhance its potential in biomedical and catalytic applications. The quinoline moiety serves as a well-established pharmacophore, widely recognized for its ability to intercalate with DNA and for exhibiting diverse biological activities, including antitumor, antibacterial, and antimalarial effects. The chloro-substituted phenol ring contributes electron-withdrawing effects that can significantly influence metal-binding affinity, lipophilicity, and cellular uptake—properties that are crucial to pharmacological performance. Meanwhile, the imine linkage facilitates strong chelation with metal centers, while also modulating redox behavior and biological reactivity, further enhancing the ligand's multifunctional character. The chosen metal ions—Cr(III), Mn(II), and Pd(II)—were selected for their distinct biological relevance and strong coordination compatibility with the tetra-dentate N,N,O,O-donor set of the investigated ligand. Their selection reflects both their diverse pharmacological potential and their ability to form stable, bioactive complexes. Cr(III) is an essential trace element involved in glucose and lipid metabolism, with reported insulin-enhancing and antioxidant properties. Mn(II) complexes are valued for their catalytic roles in redox processes, as well as their superoxide

dismutase-mimetic activity, which is linked to antioxidant and neuroprotective effects. Pd(II) is a versatile transition metal with significant applications in medicinal chemistry, particularly due to its potent cytotoxic activity and structural analogy to platinum-based anticancer agents, making it a promising candidate for chemotherapeutic development.

From this point of view, I report the sono-chemical synthesis of novel nanosized Cr(III), Mn (II), and Pd (II) complexes incorporating a chloro-2-(quinolin-8-yliminomethyl)-phenol imine ligand. The synthesized complexes are characterized using various spectroscopic and analytical techniques, including Fourier-transform infrared (FT-IR) spectroscopy, UV–Vis spectroscopy, scanning electron microscopy (SEM), and thermal gravimetric analysis (TGA). Furthermore, their biological activities, such as antimicrobial, anticancer, and antioxidant properties, are investigated, supported by molecular docking studies to elucidate their interaction mechanisms at the molecular level. The combined physicochemical and computational approach aims to provide insights into the structure–activity relationships of these novel nanosized metal complexes, paving the way for potential biomedical applications.

2. Result and Discussion

2.1. Characterization of 4-Chloro-2-(Quinolin-8-Yliminomethyl)-Phenol Ligand and Its Complexes

The solubility of the synthesized complexes was evaluated in various solvents. All complexes exhibited good solubility in polar aprotic solvents such as dimethyl sulfoxide (DMSO) and dimethylformamide (DMF), which were used for spectral and biological studies. However, they showed limited or no solubility in non-polar solvents such as hexane and toluene and moderate solubility in ethanol and methanol.

2.2. FTIR Spectrum

Infrared spectroscopy in the form of FT-IR analysis was employed to study the characteristics of the 4-chloro-2-(quinolin-8-yliminomethyl)-phenol ligand and its corresponding metal complexes, as presented in Table 1, Figure S1. A notable feature of the **L** ligand is its distinct absorption peak at 1618 cm^{-1}, which is attributed to the νC-H=N) stretching vibration. Upon interaction with chromium, manganese, and palladium ions, this peak is observed to shift to lower frequencies of 1607 cm^{-1}, 1610 cm^{-1}, and 1602 cm^{-1} for the **L-Cr**, **L-Mn**, and **L-Pd** complexes, respectively. This spectral alteration is indicative of the metal ions' chelation with the azomethine group (-CH=N) [19,20]. The ligand's FT-IR spectrum also reveals characteristic absorption bands at 1552 cm^{-1}, corresponding to the ν(C=N) mode in the quinoline moiety. After complexation with the metal species, these bands undergo a shift to lower wavenumbers: 1526 cm^{-1} for the chromium complex, 1533 cm^{-1} for the manganese complex, and 1517 cm^{-1} for the palladium complex. This phenomenon suggests the active participation of the quinoline ring in the metal coordination process [21]. Moreover, the ν(OH) stretching vibration of the free ligand at 3428 cm^{-1} diminishes, and the ν(C-O) band initially at 1269 cm^{-1} moves to lower frequencies of 1249 cm^{-1}, 1258 cm^{-1}, and 1242 cm^{-1} for the **L-Cr**, **L-Mn**, and **L-Pd** complexes, respectively. This change implies that the phenolic oxygen atom engages in C-O-M bond formation following the loss of its hydrogen atom. The appearance of novel absorption bands in the Fourier transforms infrared (FT-IR) spectra of the complexes **L-Cr**, **L-Mn**, and **L-Pd** at wavenumbers of 457 cm^{-1}, 445 cm^{-1}, and 524 cm^{-1}, respectively, can be attributed to the presence of metal–oxygen (M-O) stretching vibrations. In a similar manner, the bands observed at 513 cm^{-1}, 517 cm^{-1}, and 478 cm^{-1} for **L-Cr**, **L-Mn**, and **L-Pd** correspond to metal–nitrogen (M-N) stretching vibrations [22,23]. The specific wavenumbers and intensities of these bands provide insights into the coordination geometry and the nature of interactions surrounding the metal ions, thereby substantiating the proposed coordination models for the ligands in the metal complexes. The distinct vibrational characteristics confirm the participation of both nitrogen

and oxygen in the ligation process, which is essential for understanding the structural and bonding properties of these compounds

Table 1. The synthesized 4-chloro-2-(quinolin-8-yliminomethyl)-phenol ligand along with its metal complexes, chemical formulas, M.P, CHN, and IR frequencies.

Compounds	Empirical Formula (Formula Weight)	Color	(M. p.) and Decomp. Temp. (°C)	Λ_m (Ω^{-1} cm^2 mol^{-1})	μ_{eff} (B.M.)	Analysis (%) Found (Calc.)			IR, Cm^{-1}					
						C	H	N	(υOH)/H$_2$O	υ(CH=N)υ_{ph}	(C=N)py	υ(C-O)	υ(M-N)	υ(M-O)
L	$C_{16}H_{11}ClON_2$ (282.72)	Canary yellow	180	-	-	67.89 (67.96)	3.88 (3.92)	9.97 (9.91)	3428	1618	1552	1269	-	-
L-Cr	$C_{32}H_{22}Cl_2N_5O_6Cr$ (695.45)	Dark brown	>300	60.50	3.65	55.33 (55.27)	3.14 (3.19)	10.14 (10.07)	3359	1607	1526	1249	513	457
L-Mn	$C_{32}H_{24}Cl_2N_4O_4Mn$ (654.40)	brown	>300	8.50	5.32	58.79 (58.73)	3.76 (3.70)	8.51 (8.56)	3345	1610	1533	1258	517	445
L-Pd	$C_{18}H_{15}ClN_2O_4Pd$ (465.20)	Orange	>300	10.21	-	46.54 (46.47)	3.19 (3.25)	6.10 (6.02)	3365	1602	1517	1242	478	524

2.3. ^{1}H-NMR and ^{13}C-NMR Spectral Evaluations

The ligand in question, denoted as 4-chloro-2-(quinolin-8-yliminomethyl)-phenol, underwent comprehensive analysis via ^{1}H-NMR spectroscopy, utilizing DMSO-d$_6$ as the solvent. This analysis is presented in Figure S2. The ^{1}H-NMR spectra revealed a singlet at 13.98 ppm, which can be ascribed to the OH group of the phenolic moiety. The presence of the CH=N group was discerned at a chemical shift of 9.26 ppm. Additionally, the spectra exhibited a doublet signal at 8.83–8.80 ppm, corresponding to the hydrogen atom adjacent to the nitrogen within the quinoline ring (d, 1H, CH_{arm} adjacent nitrogen of quinoline ring). Another set of doublet signals at 8.61–8.07 ppm (d, J = 6.9 Hz, 5H, CH_{arm}) of pyridine ring in quinoline moiety and at 7.90–6.83 ppm (d, J = 7.1 Hz, 2H, CH_{arm}) and at 7.42–6.81 ppm (d, J = 7.1 Hz, 3H, CH_{arm}) was observed, attributable to the aromatic protons quinoline moiety. The ^{13}C-NMR data, obtained in DMSO-d6 medium (Figure S3), provided further structural insights with chemical shifts at 162.10 ppm for the CH=N carbons, 167.30 ppm for the CH=N carbons, 163.60 ppm for the (C-OH) carbon, 152.20 (C=N of pyridine ring in quinoline moiety), 140.50, 138.20, 134.50, 132.10, 128.70, 127.10, 125.50,124.70, 123.10, 121.10, 120.00, 115.20, and 109.50 ppm. This information collectively elucidates the molecular structure and confirms the synthesis of the ligand according to the expected chemical structure.

2.4. Elemental Analysis and Molar Conductance

The stoichiometry of the formed **L-Pd** complex with a 1:1 ratio and **L-Cr** and **L-Mn** complexes with a 2:1 ratio (L to Cr or Mn) was affirmed through elemental analysis, aligning with the anticipated proportions of carbon, hydrogen, and nitrogen, thereby confirming the adherence to their theoretical chemical formulas. Table 1 encapsulates the extensive outcomes of this research, substantiating the molecular structure of the synthesized complexes. For the L-Pd complex, this behavior can be attributed to the square-planar geometry preferred by Pd(II) ions, which coordinate with the inspected tri-dentate ligand to form a stable four-coordinate complex. The investigated Schiff base ligand acts as a tri-dentate donor, offering two nitrogen and one oxygen donor atoms, which can fully satisfy the coordination requirements of the Pd(II) center in a 1:1 molar ratio with acetate ions. Additionally, steric hindrance and electronic factors may limit the possibility of forming higher-order complexes.

The molar conductivities of the **L-Cr ([Cr(L)$_2$]NO$_3$.H$_2$O)**, **L-Mn ([Mn(L)$_2$].2H$_2$O)**, and **L-Pd** ([Pd(L)(CH$_3$COO)]·H$_2$O) complexes were determined in 10^{-3} M DMF solution. The recorded values for **L-Mn** and **L-Pd** were 8.50 Ω^{-1} cm^2 mol^{-1} and

10.21 8.50 Ω^{-1} cm^2 mol^{-1}, respectively, as indicated in Table 1. These results suggest that both **L-Mn** and **L-Pd** function as non-electrolytes [24], consistent with their low conductivity values. In contrast, the Cr(III) complex exhibits a higher conductivity of 60.50 8.50 Ω^{-1} cm^2 mol^{-1}, which is indicative of its nature as a mono-electrolyte [25].

2.5. SEM Analysis of the Prepared Nanosized Cr(III), Mn(II), and Pd(II) Metal Complexes

Scanning electron microscopy (SEM) was employed to examine the surface morphology, particle size, and structural features of the synthesized nanosized Cr(III), Mn(II), and Pd(II) metal complexes. The SEM images revealed that the complexes exhibit well-defined nanosized structures with varying morphologies influenced by the nature of the metal ion and synthesis conditions (Figure 1).

- The SEM images of the Cr(III) complex showed an aggregated but uniformly distributed morphology with spherical-like nanosized particles. The observed structures suggest a tendency for slight agglomeration due to intermolecular interactions.
- The Mn(II) complex displayed rod-like or irregular morphology, indicating variations in nucleation and growth mechanisms during sono-chemical synthesis.
- The Pd(II) complex exhibited a well-dispersed, granular, and slightly crystalline nanostructure. The smaller particle size observed for Pd(II) could be attributed to the strong coordination interactions between the Schiff base ligand and the palladium ion, stabilizing the nanostructures effectively.

The particle size of the metal complexes, estimated using ImageJ software 12 from the SEM micrographs, ranged between 25 and 45 nm with average of 36 nm for the L-Cr complex, 30–67 with average of 49 nm for the L-Mn complex and 50 and 110 nm with average 81 nm for the L-Pd complex confirming the nanoscale dimensions. The differences in morphology and size among the complexes highlight the impact of metal coordination chemistry on the self-assembly of nanosized structures. The results also indicate that the sono-chemical approach facilitated the formation of well-defined nanosized complexes with enhanced surface properties.

2.6. Electronic Absorption Spectra (EAS)

The detailed spectroscopic study of the **L** ligand, along with its complexes with **Cr(III)**, **Mn(II)**, and **Pd(II)**, was thoroughly recorded at a consistent concentration of 1×10^{-3} mol. dm^{-3} in DMF, as depicted in Figure 2 and outlined in Table S1. The ligand exhibited absorption maxima at 243 nm (ε_{max} = 1846 dm^3 mol^{-1} mm^{-1}), 256 nm (ε_{max} = 1771 dm^3 mol^{-1} mm^{-1}), and 346 nm (ε_{max} = 1836 dm^3 mol^{-1} mm^{-1}), which can be ascribed to the electronic transitions occurring between π–π* within the aromatic systems and n-π* within the heteroatom-containing aromatic structures. The absorption feature at 421 nm (ε_{max} = 1372 dm^3 mol^{-1} mm^{-1}) is indicative of an intra-ligand transition [26]. Upon complexation, new absorption bands appeared in the range of 331–325 nm, which can be attributed to π–π* transitions of the aromatic system and n–π* transitions associated with the C=N (azomethine), –CH=N–, and phenolic OH groups [27,28]. The spectral data suggests that the ligands are interacting with the respective metal ions, as evidenced by the observed shifts in band positions. The new absorption bands that appeared at 435 nm (ε_{max} = 1936 dm^3 mol^{-1} mm^{-1}) in the **L-Pd** and 383 nm (ε_{max} = 1182 dm^3 mol^{-1} mm^{-1}) in the **L-Mn** complexes are indicative of ligand-to-metal charge transfer (LMCT) transitions. These transitions likely originate from the p-orbitals of the ligands and are destined for the d-orbitals of the metal ions. Furthermore, the **L-Cr** and **L-Mn** complexes revealed an additional low-intensity broad peak at 475 nm (ε_{max} = 197 dm^3 mol^{-1} mm^{-1}) and 479 nm (ε_{max} = 1953 dm^3 mol^{-1} mm^{-1}), respectively, which was absent in the spectrum of the un-complexed ligand. This feature can be predominantly attributed to the d-d

transitions within the metal chelates' structural frameworks, which are characteristic of the metal–ligand complexation process [29].

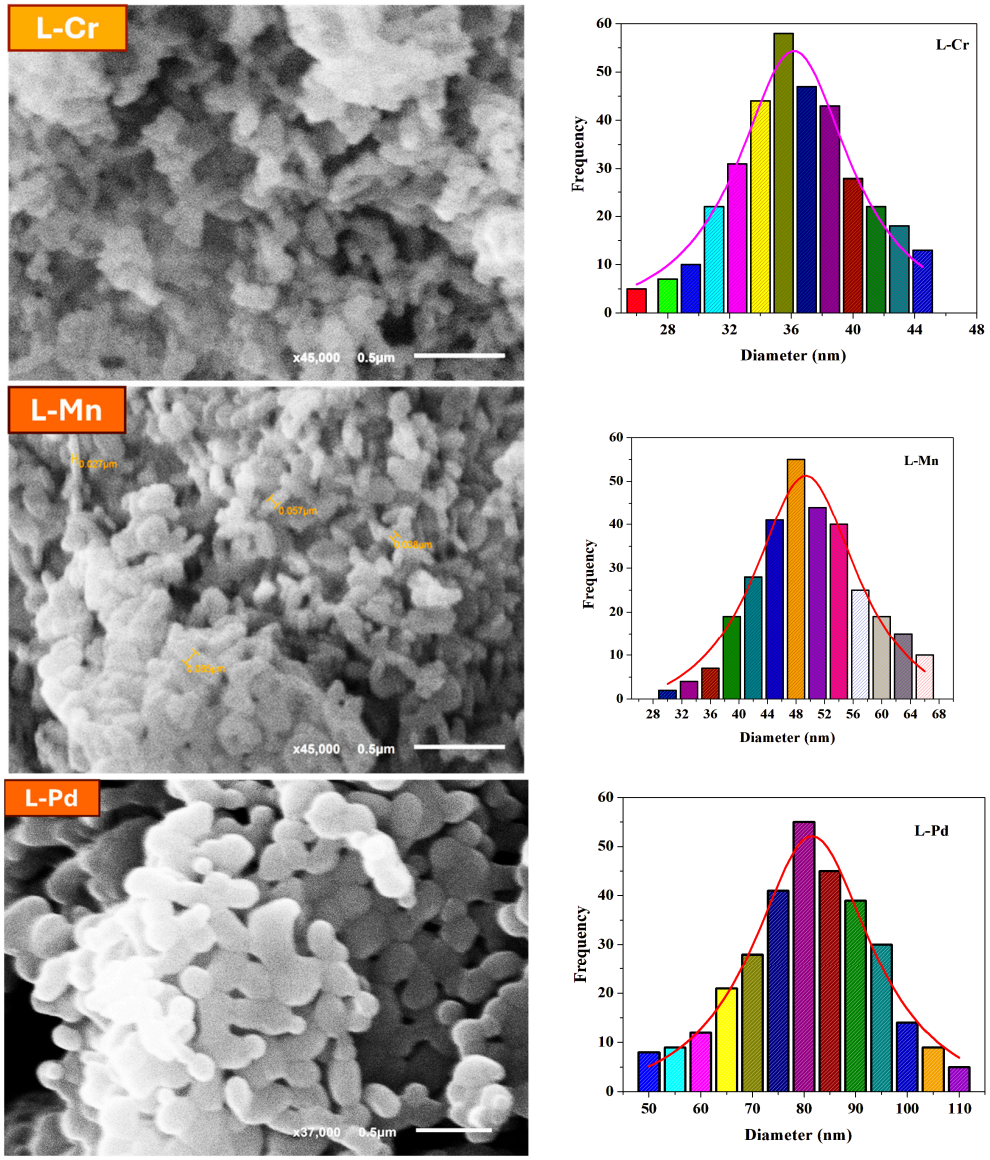


Figure 1. SEM images of the prepared nanosized metal chelates and particle size distribution for each complex.

2.7. Magnetic Moment

The magnetic moment of metal complexes provides valuable information about the electronic configuration and magnetic properties of the metal center and its surrounding ligands. The estimated magnetic susceptibility data obtained from this study closely align with the theoretical results derived from the equation $\mu_{eff} = [4S\ (S + l)]^{0.5}$. The observed magnetic data for Cr (III), Mn (II), and Pd(II) chelates with the 4-chloro-2-(quinolin-8-yliminomethyl)-phenol ligand are presented in Table 1. The findings show that the magnetic moments for the L-Cr and L-Mn complexes are 3.65 and 5.32 B.M., respectively. These values are consistent with those expected for high-spin octahedral complexes of Cr (III) and Mn (II) [30]. While the synthesized **L-Pd** complex has tetra-coordinates, resulting in a square-planar structure with diamagnetic character [31].

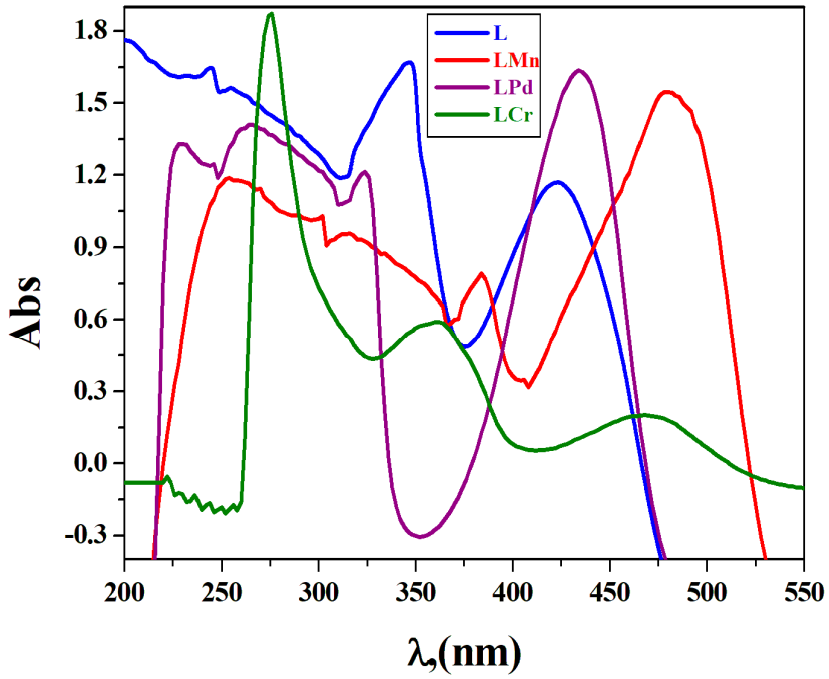


Figure 2. Electronic absorption spectra of all the prepared compounds in DMF at 298 K.

2.8. Thermal Analysis

Thermogravimetric analysis (TGA) was conducted to examine the thermodynamic stability and determine the presence of water within the crystal lattice of the synthesized compounds [32]. TGA/DTGA results for the 4-chloro-2-(quinolin-8-yliminomethyl)-phenol derived metal complexes are presented in Table 2 and Figure S4, with measurements taken between 30 °C and 800 °C. The [$C_{32}H_{22}Cl_2N_5O_6$-Cr] complex exhibits five distinct thermal degradation events. Initially, between 38 °C and 121 °C, a 2.62% mass loss occurs, which is indicative of the removal of a lattice water molecule. This is followed by an 8.96% weight reduction between 122 °C and 225 °C, corresponding to the loss of the nitrate (calc. 8.92%). The third event, at 230 °C to 305 °C, involves the elimination of a $C_9H_5NCl_2$ group with a mass loss of 28.40% (calc. 28.48%). A subsequent mass loss of 25.66% (calc. 25.59%) between 310 °C and 415 °C is attributed to the removal of a $C_{13}H_8N$ fragment. Lastly, from 420 °C to 595 °C, a $C_{10}H_7N_2O$ ligand is lost, resulting in an estimated weight decrease of 24.50% (calc. 24.58%). The ultimate residue following these degradation steps is chromium oxide. For the [$C_{32}H_{24}Cl_2N_4O_4$-Mn] complex, the TGA curve demonstrates five deterioration phases between 34 °C and 550 °C. The initial stage at 34 °C to 118 °C reveals the expulsion of two water molecules. The second phase, from 120 °C to 210 °C, corresponds to the loss of $C_7H_5Cl_2$, amounting to approximately 18.52% of the total mass (calc. 18.64%). Between 215 °C and 365 °C, a C_7H_4NO ligand is removed, contributing to a mass decrease of 19.13% (calc. 19.21%). At 370 °C to 460 °C, the TGA indicates the loss of a $C_{10}H_6N_2$ molecule, accounting for 23.60% of the mass (calc. 23.55%). Finally, the fifth stage at 465 °C to 545 °C corresponds to the degradation of a C_8H_5N unit with a mass loss of 20.70% (calc. 20.75%), leaving manganese oxide as the residue. The [$C_{18}H_{15}ClN_2O_4$-Pd] complex undergoes four weight loss stages. At the onset, from 38 °C to 125 °C, one water molecule is lost, equivalent to 3.80% of the mass (calc. 3.86%). The second stage, occurring between 125 °C and 232 °C, is associated with the removal of $C_2H_3O_2$, resulting in a 12.75% mass reduction (calc. 12.68%). The third stage, at 235 °C to 410 °C, involves the degradation of the C_7H_4NCl moiety, contributing to a 29.51% weight loss (calc. 29.55%). The last event, from 415 °C to 685 °C, corresponds to the elimination of a C_9H_6N group, with a calculated

mass loss of 27.51%, ultimately resulting in palladium oxide as the remaining product after thermal decomposition.

Table 2. Thermal decomposition steps, mass loss (%), final residue, and thermo-kinetic activation parameters.

Complexes	Temp (°C)	Fragment Loss %		Weight Loss %		E* (KJmol^{-1})	A (S^{-1})	ΔH* (KJmol^{-1})	ΔG* (KJmol^{-1})	ΔS* (Jmol^{-1}K^{-1})
		M. Formula	M. Wt.	Found	Calc					
L-Cr 695.45 Residue	38–121	H_2O	18	2.62	2.58	30.25	0.011	30.06	51.73	−270.79
	122–225	NO_3	62	8.96	8.92			29.08	79.35	−275.25
	230–305	$C_9H_5NCl_2$	198.05	28.40	28.48			28.20	104.85	−277.84
	310–415	$C_{13}H_8N$	178	25.66	25.59			27.71	130.57	−283.36
	420–595	$C_{10}H_7N_2O$	171	24.50	24.58			26.51	171.88	−286.16
	>600	CrO	68	9.85	9.77			-	-	-
L-Mn 654.40 Residue	34–118	$2H_2O$	36	5.42	5.50	49.28	0.008	48.65	69.46	−273.73
	120–210	$C_7H_5Cl_2$	160	24.55	24.46			47.91	94.14	−280.18
	215–365	C_7H_4NO	118	17.95	18.04			46.87	129.48	−284.87
	370–460	$C_{10}H_6N_2$	154	23.60	23.54			45.83	165.29	−287.85
	465–545	C_8H_5N	115	17.55	17.58			45.08	191.27	−289.48
	>550	MnO	71	10.82	10.85			-	-	-
L-Pd 465.20 Residue	38–125	H_2O	18	3.80	3.86	26.35	0.01	25.66	48.015	−272.51
	125–232	$C_2H_3O_2$	59	12.75	12.68			24.86	74.80	−279.01
	235–410	C_7H_4NCl	137.5	29.51	29.55			23.66	115.36	−283.91
	415–685	C_9H_6N	128	27.55	27.51			21.77	180.36	−288.33
	>690	PdO	122.5	26.29	26.33			-	-	-

Kinetic Parameter

The thermodynamic parameters presented in Table 2 exhibit variations with respect to temperature. Specifically, the observed increase in G* values is indicative of a positive temperature coefficient, suggesting a rise in the rate of the degradation process as temperature escalates. This is consistent with the interpretation that higher temperatures are conducive to the activation of the system, thereby promoting the degradation reaction. The magnitude of the H* values, being positive, underscores the endothermic nature of the degradation. This implies that the reaction absorbs heat from its surroundings as it proceeds, which is characteristic of endothermic reactions that require additional energy to overcome the activation energy barrier. Concerning the entropy of activation (S*), most steps in the thermal degradation process exhibit negative values. This negative S* implies that the activated complex is more ordered than the reactants, which is indicative of a decrease in entropy during the reaction. This observation can be rationalized by considering that the degradation may occur through an abnormal mechanism, where the breakdown of molecular structures leads to a more ordered state at the intermediate stages. The negative values of S* can also be linked to the chemisorption of oxygen and the presence of other decomposition byproducts. The interaction of these species with the substrate may induce a more organized arrangement of molecules within the activated state, contributing to the reduced entropy. This ordered state is believed to facilitate the bond-breaking and bond-making processes necessary for degradation, thereby lowering the overall activation entropy. The nature of the activated state's increased order can be understood in terms of bond polarization. As the system transitions from reactants to the activated complex, there may be significant electronic rearrangements that lead to a more polarized state. These electronic transitions are essential for the cleavage of bonds and the formation of new ones, which are fundamental steps in the degradation process [33].

2.9. Stoichiometry of Complexes in Solution

Employing the techniques of continuous variation and molar ratio analysis, the stoichiometry of the synthesized complexes was ascertained [34–37]. The continuous variation graph revealed an absorbance peak at a ligand mole fraction range of 0.51–0.62, indicating

the formation of complexes where Cr(III) and Mn(II) ions bind to the ligand in a 1:2 molar ratio and Pd(II) ion in a 1:1 molar ratio (Figure 3). This observation was corroborated by the molar ratio plot, which also affirmed these specific stoichiometric relationships between the metal ions and the ligand (Figure S5).

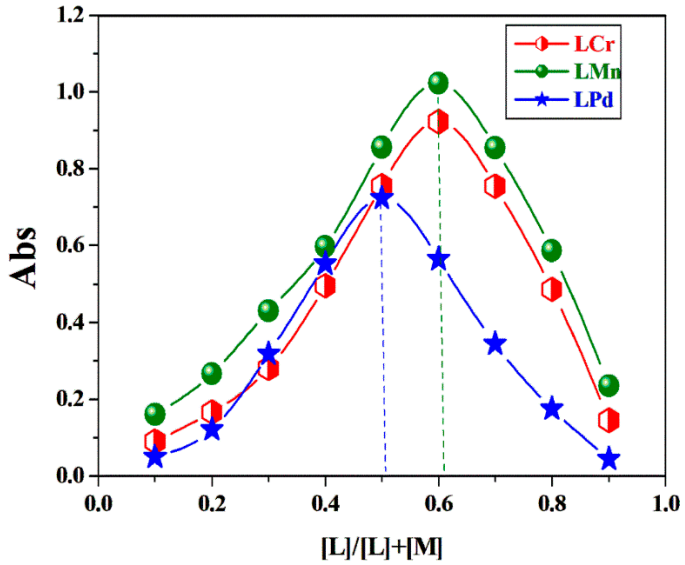


Figure 3. Continuous variation plots for the prepared complexes in DMF at [complex] = 1×10^{-3} M and 298 K.

2.10. The Apparent Formation Constants of the Synthesized Complexes

Evaluation of the Synthesized Complex Formation Constants: The synthesized complexes' formation constants (Kf) were derived from spectrophotometric data using the continuous variation technique, as presented in Table 3. The results indicate that the complexes exhibit substantial stability, with the order of stability being **L-Mn** > **L-Cr** > **L-Pd** complexes. Additionally, the stability constants (pK) and Gibbs free energy (ΔG*) values were determined for these complexes. The calculated ΔG^* values are negative, suggesting that the complexation reactions occur spontaneously and are energetically favorable [35].

Table 3. The formation constant (K_f), stability constant (-log K_f), and Gibbs free energy (ΔG*) values of the prepared complexes in aqueous ethanol at 298 K.

Complexes	K_f	pK	$\Delta G^{\neq}$ kJ mol^{-1}
L-Cr	4.75×10^7	7.67	−43.99
L-Mn	6.18×10^7	7.79	−44.45
L-Pd	4.87×10^4	4.69	−26.67

2.11. pH Profile of the Investigated Complexes

The analysis of complex stability in relation to pH was conducted through spectrophotometry, which entailed measuring the absorbance of the complexes across an extensive pH spectrum from 2 to 12. The characteristic absorption bands corresponding to the metal–ligand charge transfer (LMCT) in the L-Pd complex and d-d transition in the L-Mn and L-Cr complexes were used to assess the pH dependence. This research aimed to establish the exact pH intervals wherein the complexes maintain their structural integrity, thereby ascertaining their operational effectiveness across a variety of environmental pH conditions, which is essential for their intended functionality. The stability curve presented in Figure 4 reveals that these complexes demonstrate persistent steadiness within a pH window of 4 to

11. Given this stability profile, it is anticipated that the complexes will function effectively in surroundings where the pH is contained within these bounds [38].

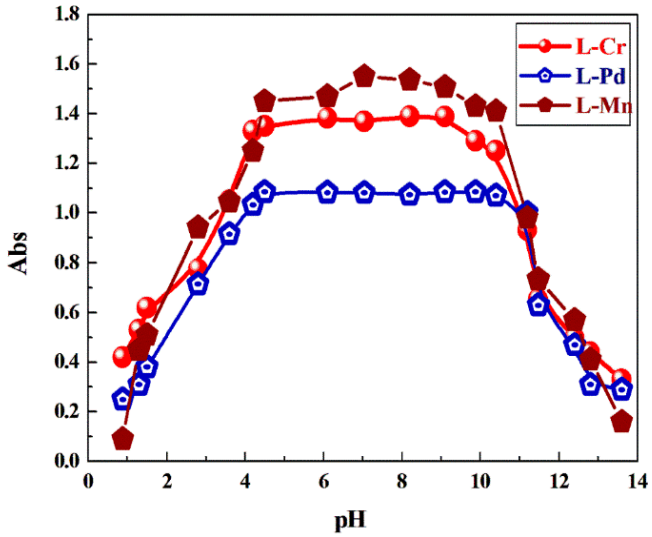


Figure 4. The effects of pH on the complexing elements in aqueous ethanolic media at 25 °C.

2.12. DFT Details

2.12.1. Geometry Optimization and Mulliken Charge

The geometry optimization of the L, L-Pd, L-Mn, and L-Cr compounds was performed using the DFT/B3LYP method in the gas phase. For this analysis, the 6-311g (d,p) basis set was applied to lighter atoms (C, H, N, Cl, and O), while the LANL2DZ basis set was used for the heavier atoms (Pd, Mn, and Cr). The optimized configurations for L, L-Pd, L-Mn, and L-Cr yielded minimum energies of −1261.48, −1616.22, −2625.44, and −2607.80 Hartree, respectively. These findings suggest that the metal complexes exhibit better stability energy than the free L. The calculated dipole moment values for L-Pd, L-Mn, and L-Cr are 9.45, 5.72, and 5.70 Debye, respectively, all of which are higher than the dipole moment of the free L, which is 4.33 Debye. These results show the strong dipole–dipole interactions within the metal chelates [39], emphasizing their crucial influence on both the structural and electronic properties of the systems. The optimized ground-state geometries of the compounds, along with key atomic numbering, are depicted in Figure 5. DFT analysis reveals that in the L-Pd complex, the metal ion coordinates with the O1, O2, N1, and N2 atoms, forming a square-planar structure. In contrast, the L-Mn and L-Cr complexes coordinate with the N1, N2, N3, and N4 atoms, as well as two oxygen atoms (O1 and O2), leading to the formation of an octahedral geometry. The Mulliken charge distribution offers important insights into the potential coordination sites of the ligand (L), helping to identify its chelating centers. By examining the gas-phase optimized geometry, the Mulliken charges of key atoms in L were determined. The atomic charges for N1 (−0.315), N2 (−0.451), and O1 (−0.348) were found to be negative, suggesting a strong tendency for electrophilic interactions. These negative charges indicate that these atoms are ideal coordination sites, facilitating the chelation of metal ions such as Pd^{2+}, Mn^{2+}, and Cr^{3+}.

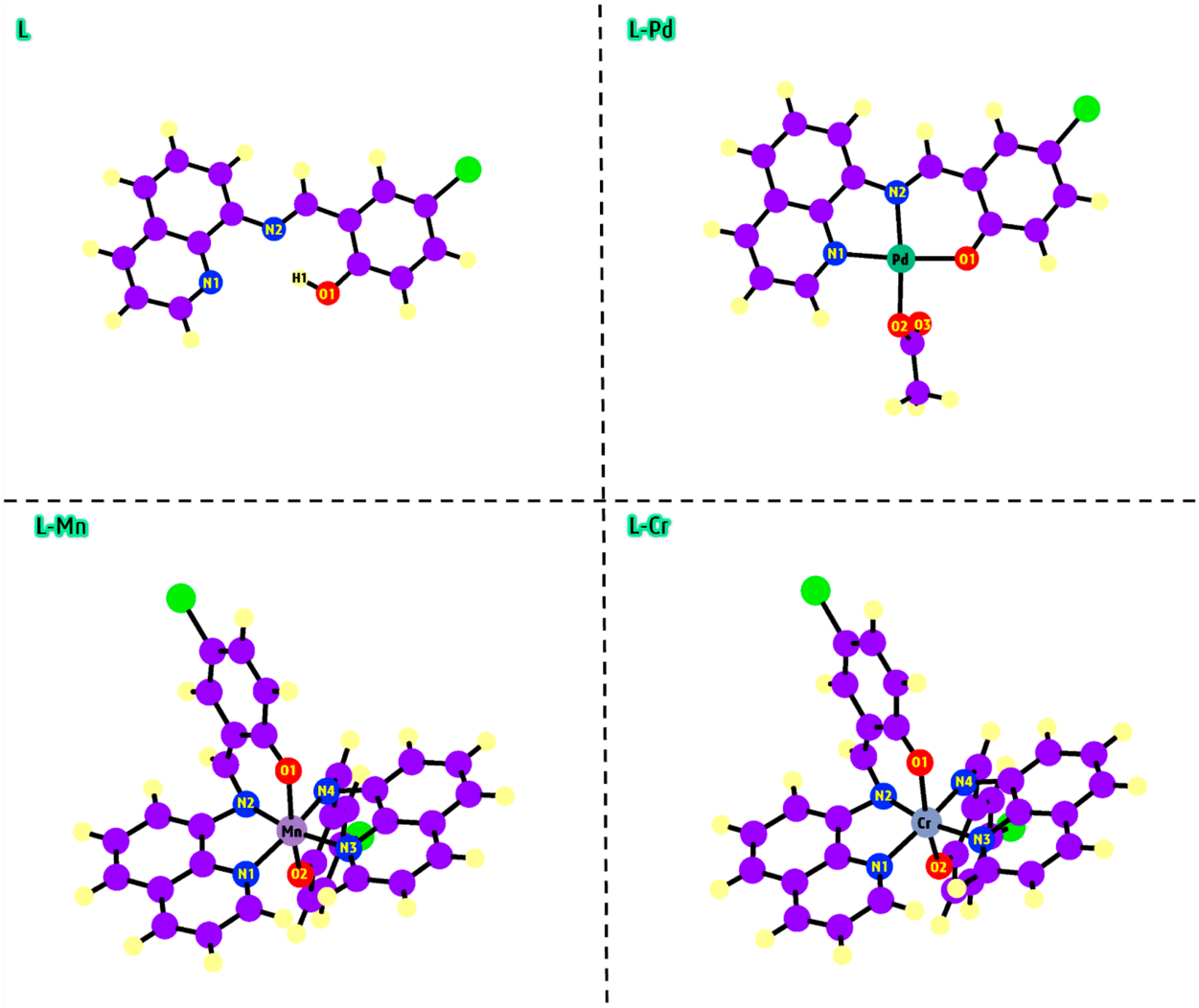


Figure 5. The proposed geometry of L, L-Pd, L-Mn, and L-Cr compounds by computational approach.

2.12.2. Electrophilic and Nucleophilic Reaction Sites

The MEP, known as the molecular potential surface map, is a valuable tool for analyzing charge-dependent interactions such as electrophilic and nucleophilic reactions, hydrogen bonding, and overall charge distribution within molecules. It also serves as an effective method for identifying reactive sites within a molecule [40]. The MEP maps of L, L-Pd, L-Mn, and L-Cr are illustrated in Figure 6, with color-coded representations indicating varying electrostatic potential levels. Typically, the electrostatic potential follows an increasing trend in the order: red < orange < yellow < green < blue [41]. In the visualization, green represents regions of neutral potential, yellow indicates areas with a slight electron density, and blue highlights nucleophilic zones with a higher positive charge distribution [42]. The MEP map of the L compound reveals a significant negative potential concentrated in the central region, specifically between the N1, N2, and O1 atoms. This area, highlighted in red, indicates a strong electrophilic reaction site, suggesting its potential role in interactions with positively charged species [43–45] such as Pd^{2+}, Mn^{2+}, and Cr^{3+}. These results align with the Mulliken charge distribution analysis, further confirming the active sites of the ligand (L) responsible for chelation with metal ions. In the L-Pd complex, the negative potential is predominantly concentrated around the O3 atoms, indicating that this region is highly favorable for electrophilic reactions and hydrogen bonding interactions. The MEP maps of the L-Mn and L-Cr complexes exhibit a comparable distribution, indicating similar regions of electrophilic and nucleophilic reactivity. The potential energy range for L, L-Pd,

L-Mn, and L-Cr is −0.59 to +0.59 a.u., −1.06 to +1.06 a.u., −0.65 to +0.65 a.u., and −0.64 to +0.64 a.u., respectively.

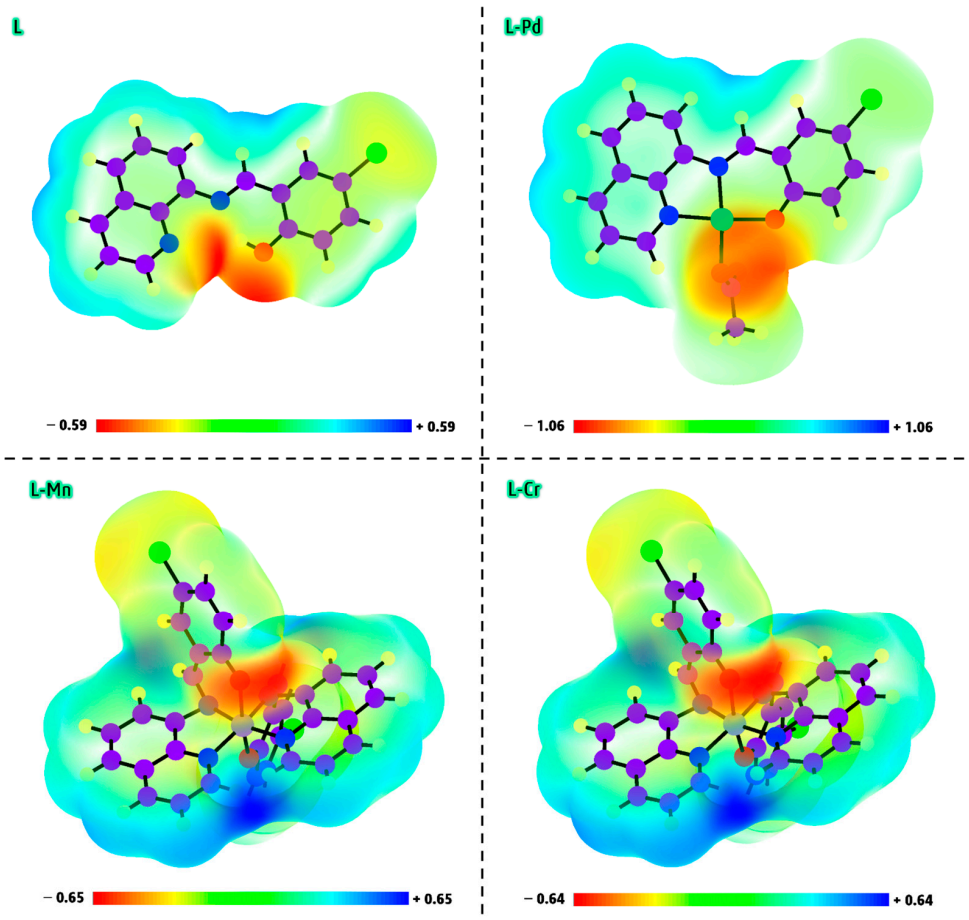


Figure 6. The MEP demonstration of L, L-Pd, L-Mn, and L-Cr compounds by computational approach.

2.12.3. Molecular Orbital Analysis

The HOMO and LUMO are key frontier orbitals that define a molecule's electronic properties and reactivity. These orbitals, representing the outermost boundaries of a molecule's electronic structure, play a fundamental role in various chemical reactions, particularly those involving electron transfer. HOMO is critical in electron-donating and nucleophilic reactions, as molecules with an intermediate HOMO energy serve as effective electron donors, readily participating in nucleophilic or oxidative processes. Conversely, LUMO represents the lowest accessible energy level for incoming electrons (Figure 7). Molecules with a low LUMO energy are excellent electron acceptors, making them highly reactive in electrophilic interactions. A crucial factor in molecular chemistry is the HOMO–LUMO energy gap. A smaller gap indicates higher reactivity, as the molecule requires less energy for excitation, enhancing its ability to engage in chemical transformations. The calculated energy values for L, L-Pd, L-Mn, and L-Cr are 3.72, 1.34, 2.71, and 2.66 eV, respectively. These findings suggest that the L-Pd complex exhibits the highest biological activity and chemical reactivity among the studied compounds. The observed trend in biological activity and reactivity follows the order of L-Pd > L-Cr > L-Mn > L, while the stability trend is reversed, following the sequence of L > L-Mn > L-Cr > L-Pd. Furthermore, the smaller energy gap of the Pd(II) complex enhances the efficiency of intramolecular charge transfer (ICT) along conjugated pathways. This facilitates electron transfer from electron-donating groups to electron-accepting groups within the molecule [46], thereby improving its electronic properties and reactivity. On the other hand, a smaller HOMO–LUMO

gap typically indicates that the complex requires less energy for electronic transitions, thereby facilitating redox processes. The L-Pd complex, with its reduced HOMO–LUMO gap, is likely to possess a higher redox potential, making it more susceptible to electron exchange. This energy gap suggests that the L-Pd complex could exhibit enhanced redox activity, which may have important implications for its catalytic, electrochemical, or biological properties.

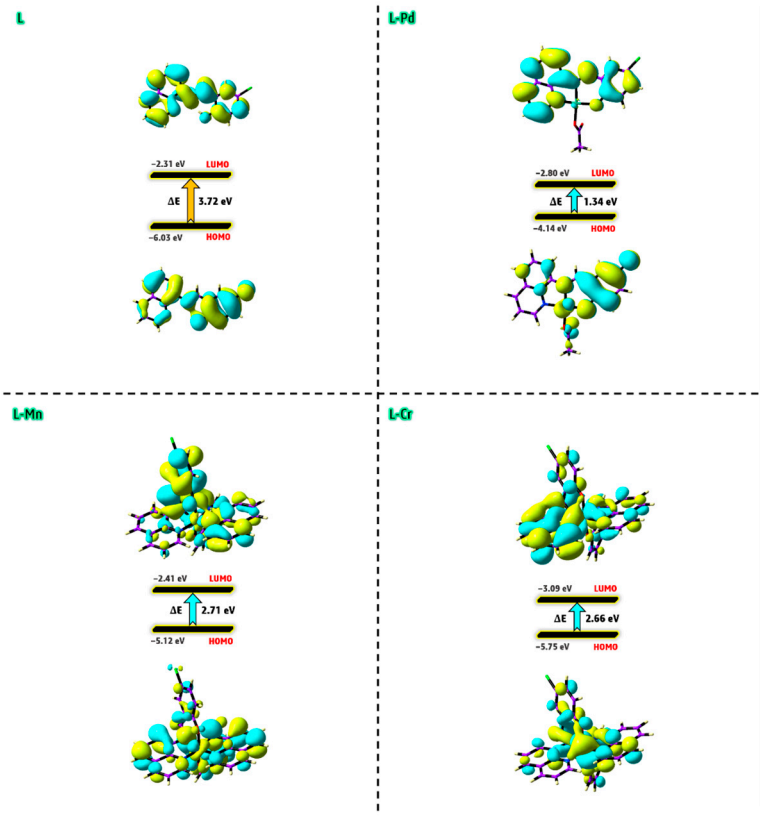


Figure 7. The predicted HOMO and LUMO contours of L, L-Pd, L-Mn, and L-Cr compounds.

2.12.4. Physicochemical Parameters

The energy values of the HOMO and LUMO in the compounds are essential for calculating several quantum indices, including chemical potential (P_i), maximum electronic charge transfer (ΔN_{max}), global electrophilicity (ω), absolute electronegativity (χ), absolute hardness (η), and absolute softness (σ). These parameters were derived using a series of mathematical equations, as outlined in Equations (1)–(6) [47].

$$Pi = -\chi \quad (1)$$

$$\chi = \frac{-(E_{HOMO} + E_{LUMO})}{2} \quad (2)$$

$$\eta = \frac{E_{LUMO} - E_{HOMO}}{2} \quad (3)$$

$$\sigma = \frac{1}{\eta} \quad (4)$$

$$\omega = \frac{Pi^2}{2\eta} \quad (5)$$

$$\Delta N_{max} = \frac{-Pi}{\eta} \quad (6)$$

Table 4 shows the values of the physicochemical parameters for the L, L-Pd, L-Mn, and L-Cr compounds, derived from the E_{HOMO} and E_{LUMO} values. A comprehensive analysis of the data provides valuable insights, highlighting key trends and characteristics of the L, L-Pd, L-Mn, and L-Cr compounds as follows:

(i) The degree of electron transfer within a compound can be assessed using the additional electronic charge parameter (ΔN_{max}), which measures a molecule's tendency to accept electrons from another species. Based on this parameter, the results suggest that the L-Pd, L-Mn, and L-Cr complexes possess enhanced electron transfer capabilities compared to the free ligand (L). Among these, the Pd(II) complex exhibits the highest electron-accepting ability, highlighting its superior electronic properties.

(ii) Balancing a compound's chemical reactivity with its hardness or softness is essential in determining its interaction potential. The Hard-Soft Acid-Base (HSAB) principle offers valuable insights into molecular reactivity, suggesting that hard acids preferentially bind to hard bases, while soft acids form more stable interactions with soft bases. In biological systems, key components such as cells and proteins are classified as soft molecules, making them more likely to interact with other soft molecules rather than hard ones. This explains why softer chemical environments generally enhance biological activity, whereas harder environments tend to suppress it [48]. Based on chemical hardness and softness parameters, the predicted reactivity trend for the studied compounds follows the order of L-Pd > L-Cr > L-Mn > L (Table 4), indicating that L-Pd exhibits the highest reactivity among them.

(iii) The global electrophilicity index (ω) quantifies a molecule's ability to accept electrons, classifying it as strong (ω > 1.5 eV), moderate (0.9 eV < ω < 1.4 eV), or marginal (ω < 0.8 eV). The electrophilicity index values for the studied metal complexes range from 5.23 to 8.98 eV, confirming their strong electrophilic nature. This result suggests that these complexes possess significant reactivity, which may contribute to their potential biological activity [49].

Table 4. Physicochemical parameters for the L, L-Pd, L-Mn, and L-Cr compounds.

Parameter	L	L-Pd	L-Mn	L-Cr
E_{HOMO}	−6.03	−4.14	−5.12	−5.75
E_{LUMO}	−2.31	−2.80	−2.41	−3.09
$\Delta E_{(LUMO–HOMO)}$	3.72	1.34	2.71	2.66
χ	4.17	3.47	3.76	4.42
η	1.86	0.67	1.35	1.33
σ	0.53	1.49	0.74	0.75
P_i	−4.17	−3.47	−3.76	−4.42
ω	4.67	8.98	5.23	7.34
ΔN_{max}	2.24	5.18	2.78	3.32

Analyzing these parameters provides valuable insights into the reactivity, stability, and intermolecular interactions of molecules, along with their electrical and optical properties. This deeper understanding enables the development of novel materials with enhanced characteristics while also optimizing existing ones for a wide range of applications.

The DFT calculations presented in this study play a critical role in elucidating the electronic and structural features that govern the reactivity and biological behavior of the synthesized compounds. Key parameters such as HOMO–LUMO energy gaps, Mulliken charge distribution, molecular electrostatic potential (MEP), and global reactivity descriptors (electrophilicity, chemical hardness, and charge transfer capacity) offer detailed insights into the stability, coordination behavior, and potential interaction sites of the ligand and its metal complexes. Notably, the enhanced reactivity and biological affinity of the

L-Pd complex can be rationalized by its low energy gap, high electrophilicity, and significant softness—attributes that align closely with its superior docking performance and experimental activity. These computational results, therefore, provide a predictive and mechanistic foundation that complements and substantiates our experimental findings.

2.13. Molecular Modeling

Molecular modeling is essential for accurately visualizing and predicting ligand–target interactions, making it a powerful tool for validating experimental results. In this study, molecular docking simulations were performed to reinforce the observed anticancer, antimicrobial, and antifungal properties of the synthesized compounds. The key docking representations highlighting their biological activity are summarized below.

To evaluate the antimicrobial potential of the compounds, the optimized structures were docked into the active site of 4EWP for *Micrococcus luteus* bacteria. Figure 8 provides a detailed visualization of the docking poses within the active site of 4EWP, along with the corresponding 3D interaction diagrams. The analysis revealed significant interactions with key amino acids, highlighting their potential effectiveness against microbial targets. According to the docking results, the free binding energies for L, L-Pd, L-Mn, and L-Cr were calculated as −6.67, −9.33, −8.63, and −8.68 kcal/mol, respectively. These findings indicate that the L-Pd complex exhibits the strongest binding affinity to the protein's active site compared to the other compounds, verifying the strong effect of this complex in the inhibition of *Micrococcus luteus*. The L-Pd complex establishes seven hydrophobic interactions between its aromatic rings and key amino acid residues of 4EWP, including ALA 338, LEU 236, MET 202, VAL 92, and VAL 156. Additionally, two hydrophobic interactions occur between a chlorine atom in the complex and the amino acids VAL 156 and PRO 95. Furthermore, a hydrogen bond is observed between the O1 atom and GLN 206, while a halogen bond is formed between the chlorine atom and THR 93.

To evaluate the anticancer potential of the compounds, molecular docking simulations were conducted using the 3HB5 breast cancer protein as the target. During the molecular docking process, L, L-Pd, L-Mn, and L-Cr were docked into the active site of 3HB5. The binding affinity values obtained were −6.78, −8.35, −6.98, and −7.03 kcal/mol, respectively. These results suggest that the L-Pd complex exhibits the strongest binding interaction with the target protein, indicating its potential for enhanced biological activity against breast cancer cells. A stronger interaction corresponds to a more negative binding energy. Accordingly, the binding strength follows the order of L-Pd > L-Cr > L-Mn > L. This trend aligns well with the experimental findings, further validating the computational results. The docking representation, along with the corresponding 3D interaction diagrams for the binding process of L, L-Pd, L-Mn, and L-Cr with 3HB5, is illustrated in Figure 9. The L-Pd complex forms five hydrophobic interactions between its aromatic rings and crucial amino acid residues of the breast cancer protein, including ILE 14, VAL 188, PHE 192, and PRO 187. Additionally, a chlorine atom in the complex engages in two hydrophobic interactions with LEU 149 and VAL 143. Moreover, two hydrogen bonds are established between the complex and the SER 142 and CYS 185 residues, further reinforcing its binding stability.

Our in vitro studies demonstrated the remarkable efficacy of these metal chelates in inhibiting fungal growth. To gain deeper insights into their mechanism of action, docking simulations were performed to analyze their molecular interactions in detail. The docking analysis specifically targeted the active site of *Candida albicans* (PDB code: 5V5Z), providing a comprehensive understanding of their antifungal properties. The binding free energy values of L, L-Pd, L-Mn, and L-Cr within the active site of *Candida albicans* were determined to be −7.16, −10.56, −8.26, and −10.35 kcal/mol, respectively. Notably, the L-Pd complex demonstrated the highest binding affinity, suggesting its potential for strong interactions

and effective inhibition of *Candida albicans*. Figure 10 demonstrates the interaction diagrams between L, L-Pd, L-Mn, and L-Cr and the active site of *Candida albicans*. The L-Pd complex establishes three hydrogen bonds with the amino acid residues CYS 470, GLY 472, and ILE 471 through the O3 atom. Additionally, fifteen hydrophobic interactions were identified between the Pd(II) complex and the amino acid residues ILE 131, LEU 300, ILE 304, LEU 204, LEU 276, ALA 149, LEU 150, ALA 146, and LYS 143, demonstrating its strong binding affinity and potential stability within the biological system.

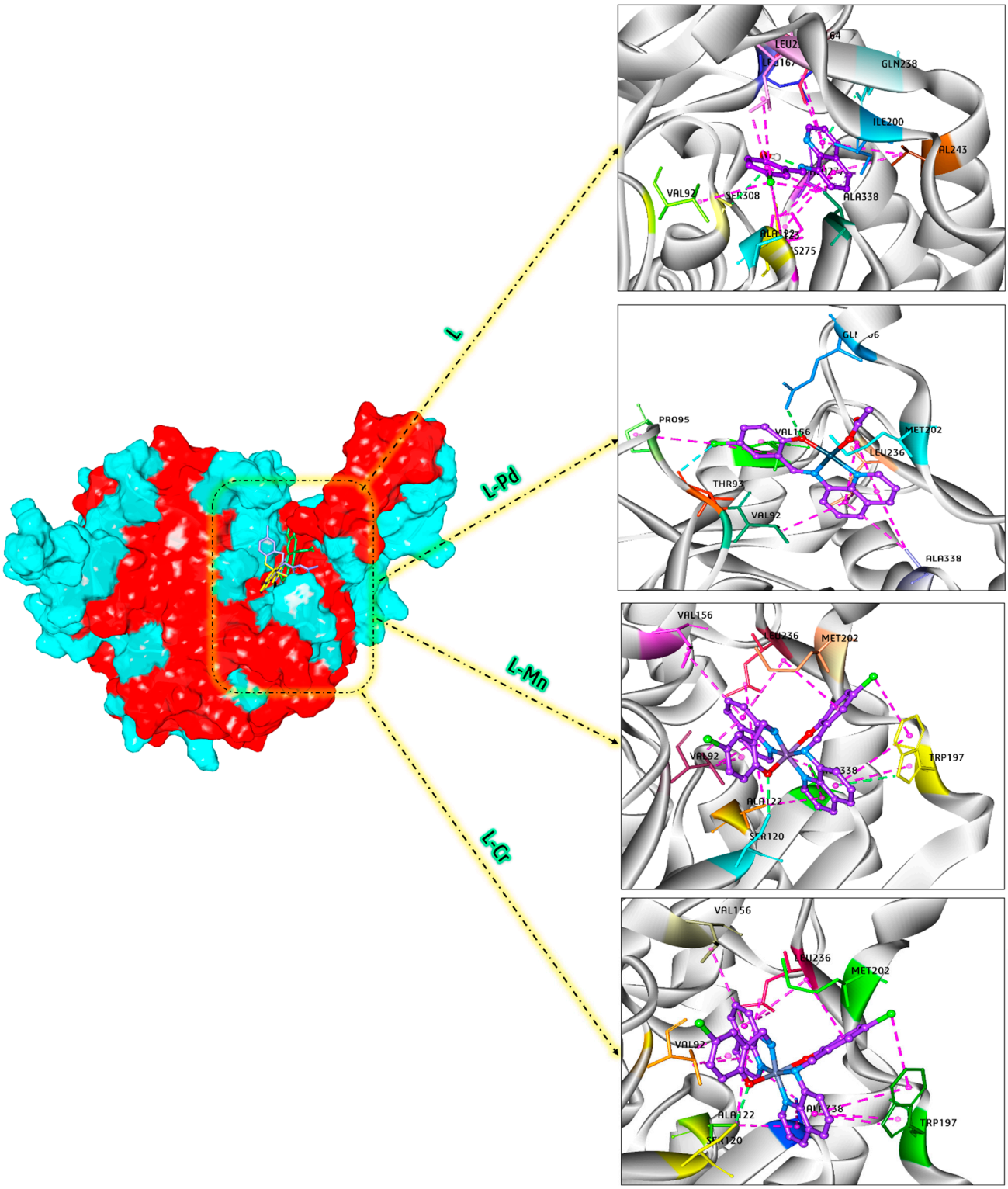


Figure 8. Docking analysis of L, L-Pd, L-Mn, and L-Cr in the interaction with the 4EWP target.

Theoretical calculations indicate that the studied chelates possess small energy gap values, suggesting their potential for efficient charge transfer to breast cancer protein, *Micrococcus luteus*, and *Candida albicans*. Additionally, the high global electrophilicity index further confirms the enhanced reactivity of these compounds toward these biological targets. Consequently, all DFT parameters validate the superior biological activity of the L-Pd complex, as corroborated by both molecular docking and experimental findings.

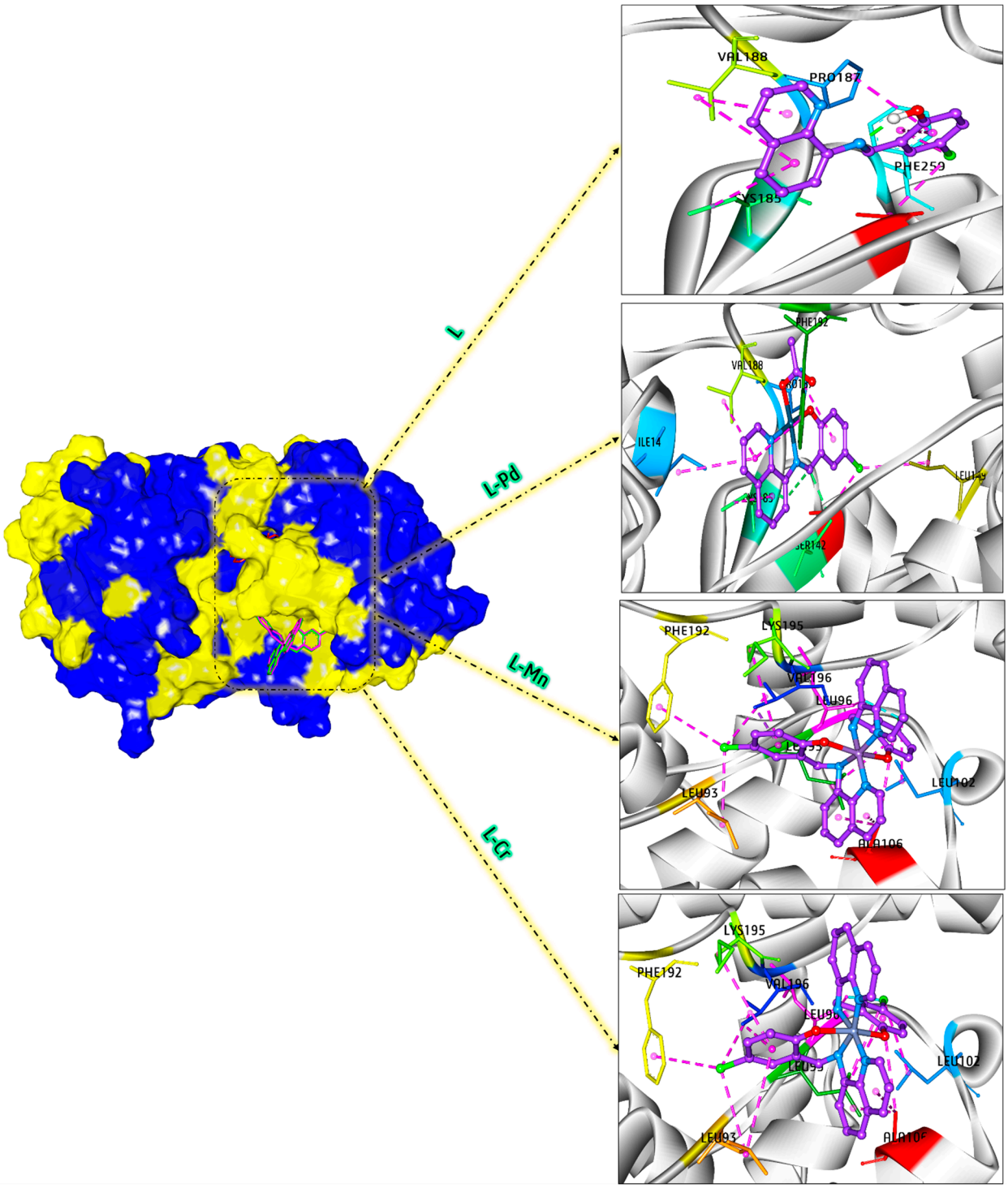


Figure 9. Docking analysis of L, L-Pd, L-Mn, and L-Cr in the interaction with the 3HB5 target.

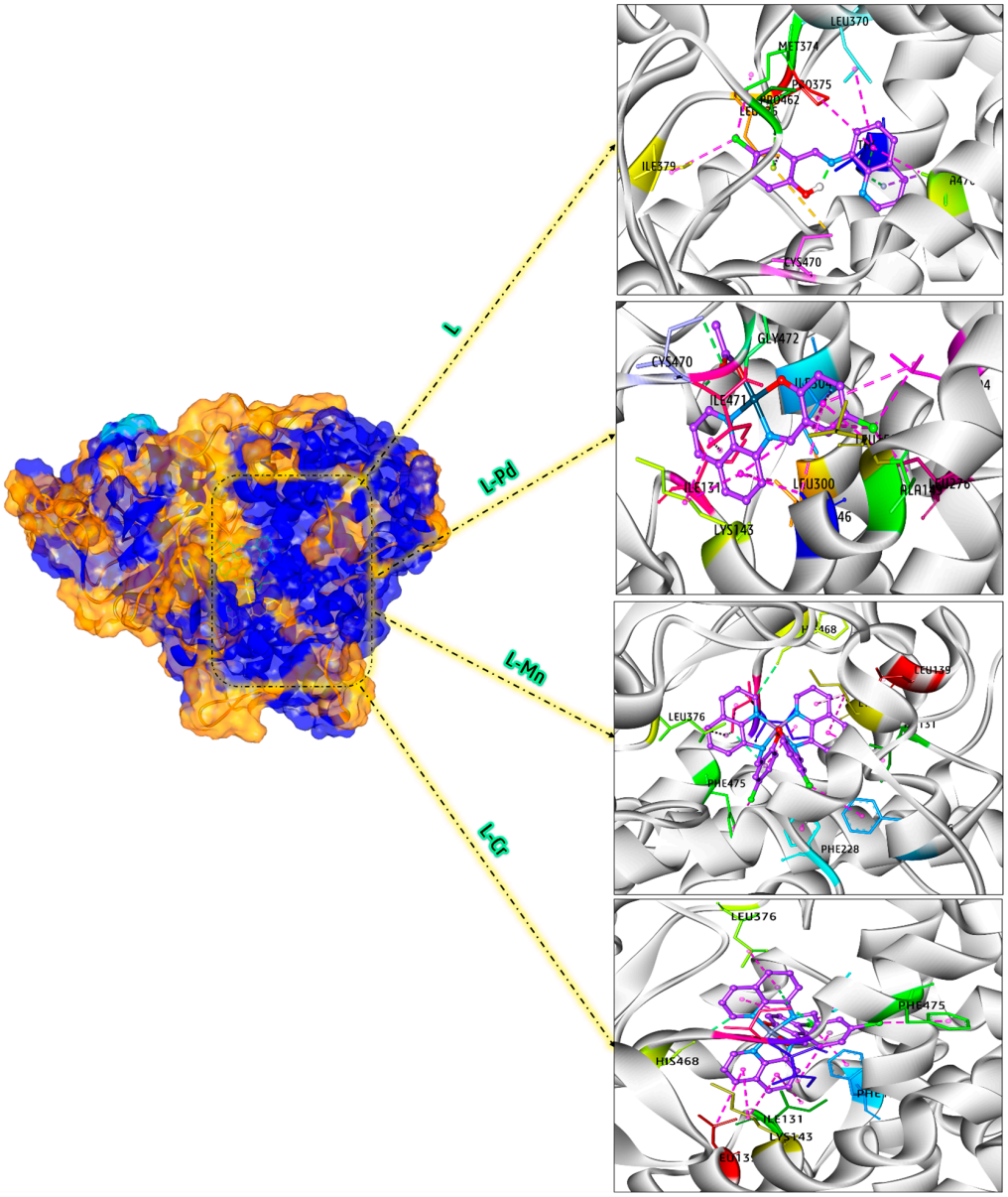


Figure 10. Docking analysis of L, L-Pd, L-Mn, and L-Cr in the interaction with the 5V5Z target.

2.14. Biological Activity

2.14.1. Antimicrobial Activity

The study evaluated the antimicrobial properties of a synthesized 4-chloro-2-(quinolin-8-yliminomethyl)-phenol ligand and its corresponding metal complexes against specific bacterial strains, including *S. marcescens*, *M. luteus*, and *E. coli*, as well as fungi such as (*A. flavus*, *C. candidum*, and *F. oxysporum*). Ofloxacin and fluconazole were employed as benchmarks for antibacterial and antifungal activities, respectively. The ligand–palladium complex (**L-Pd**) exhibited the most significant antimicrobial effect among the compounds examined, as indicated by the inhibition zone diameter measurements (mm/μg of sample). This enhanced activity in the metal complexes is likely attributed to chelation theory, which suggests that the formation of a chelate complex can increase the biological efficacy of the ligand by improving its ability to interact with biological targets [50,51]. The varying antimicrobial potencies observed may be a result of differences in the cellular structure, particularly the cell wall composition, of the microbial species under study [52]. The minimum concentration required to inhibit the growth of the microorganisms (MIC) for the synthesized compounds is presented in Table 5. Additionally, to affirm the accuracy of

the antimicrobial assessment, an activity index calculation was performed, as outlined in Table 6. It is important to note that the concentration of dimethyl sulfoxide (DMSO) used in the preparation of these samples did not surpass 0.5%, ensuring that it would not interfere with the experimental outcomes [53]. The actual inhibition zones for both bacterial and fungal species are detailed in Tables S2 and S3 of the Supplementary Materials.

Table 5. The results of the minimum inhibition concentration (MIC) of the ligand and its metal complexes against the different strains of bacteria and fungi.

Compound	(MIC) Minimum Inhibition Concentration µg/mL					
	Bacteria			Fungi		
	S. marcescence	*E. coli*	*M. luteus*	*A. flavus*	*C. albicans*	*F. oxysporum*
L	7.5	8.25	6.5	8.75	6.25	7
L-Cr	2.75	3.5	2	3.75	2.25	3.25
L-Mn	3	3.75	2.5	4	3	3.75
L-Pd	2.25	3	1.75	3	2.25	2.75
Ofloxacin	2	2.75	1.5			
Fluconazole				2.25	1.75	2.5

Table 6. Antimicrobial activity index (%) of the ligand and its complexes.

Compound	Activity Index (%)					
	Bacteria			Fungi		
	S. marcescence	*E. coli*	*M. luteus*	*A. flavus*	*C. albicans*	*F. oxysporum*
L	44.05	38.48	37.7	39.41	34.96	33.65
L-Cr	94.82	91.58	95.06	92.87	94.09	91.23
L-Mn	89.94	86.97	93.22	88.26	91.26	86.28
L-Pd	97.71	98.2	98.74	96.23	95.37	95.85

2.14.2. Determination of Minimum Inhibition Concentration

The outcomes from the serial dilution assay (MIC) exhibit a strong congruence with the results obtained via the disk diffusion method, as depicted in Table 5 and Figures 11 and 12. In contrast to other complexes examined, the **L-Pd** complex has demonstrated remarkable bio-efficiency, with MIC values of 2.25, 3.00, and 1.75 M against *S. marcescens*, *E. coli*, and *M. luteus*, respectively. Amongst the bacterial species under study, *M. luteus* emerged as the most susceptible, while *E. coli* displayed the highest resilience. Notably, *G. candidum* was identified as the most sensitive fungus. This enhancement in antimicrobial potency can be rationalized in light of Overtone's principles [54–56], which suggest that chelation enhances the ligand's function as a more potent antibacterial agent by constraining bacterial proliferation. The significant increase in the inhibitory zones of metal chelates versus free ligands is indicative of the metal's ability to interact more effectively with biological targets due to the reduced polarity resulting from the shared positive charge with the ligand's hetero atoms and the delocalization of π electrons throughout the chelate framework. The bacterial cell wall and membrane, rich in lipids and polysaccharides, provide an optimal environment for metal ion interaction. The varying sensitivity of different bacteria to these complexes may be attributed to differences in their ribosomal structure or cellular permeability. Moreover, the metal complexes' effectiveness could be influenced by factors such as solubility, size, dipole moment, metal ion redox potential, bond length, complex geometry, and hydrophobicity. The steric hindrance may also affect their antimicrobial activity since limited lipid solubility can impede the metal ion's ability to reach the cell wall's active site, thereby hindering the complexes' antibacterial efficacy. The data suggest that the antibacterial performance of metal complexes is not solely determined by chelation but is

instead a multifaceted phenomenon influenced by a confluence of factors. These include the complex's solubility, the metal–ligand bond length, the metal ion's redox state, its spatial arrangement within the complex, the molecule's overall shape, and the physicochemical properties that govern its interaction with bacterial membranes and subsequent cell penetration. Additionally, pharmacokinetic factors such as concentration and the molecule's tendency to partition between hydrophilic and hydrophobic environments contribute to the overall antimicrobial efficacy. Thus, the observed increase in antibacterial activity of metal complexes can be ascribed to a composite of various mechanisms beyond chelation, which may interact synergistically to inhibit microbial growth [57,58].

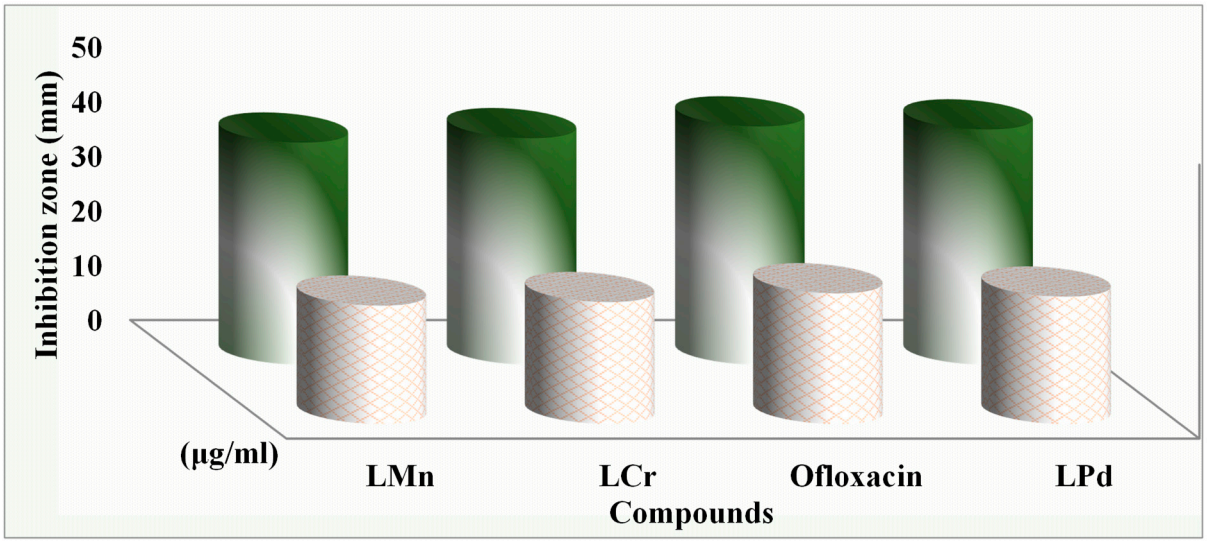


Figure 11. Antibacterial activity for the compounds under inspection against *M. luteus* bacteria.

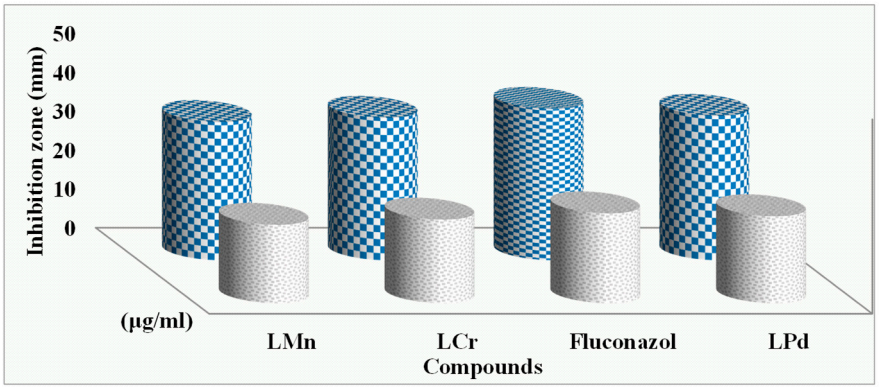


Figure 12. Antifungal activity for the compounds under inspection against *C. albicans* fungi.

2.15. Anti-Cancer

The study examined the antitumor properties of the 4-chloro-2-(quinolin-8-yliminomethyl)-phenol ligand and its associated complexes with Cr(III), Mn(II), and Pd(II) metals in HepG-2, HCT-116, and MCF-7 cell lines using IC_{50} values (Table S4 and Figure 13). It was found that both the ligand and its metal derivatives suppressed cell proliferation in a dose-dependent manner, although their efficiencies varied significantly (as depicted in Figure 13). Upon analysis of the IC_{50} values (Table S4), it was determined that all metal complexes exhibited stronger inhibitory effects than the ligand alone. Notably, the Pd(II) complex displayed the highest potency, with IC_{50} values of 3.82 and 4.17 µg/µL against MCF-7 and HepG-2 cells, respectively, which were comparable to the reference drug Cisplatin at 10.75 and 6.65 µg/µL. This suggests that the **L-Pd** complex

holds promise as a potential treatment for hepatic tumors. Additionally, the **L-Cr** complex demonstrated substantial inhibitory activity against the MCF-7 cell line, with an IC_{50} value of 5.86 μg/μL. The relative cytotoxic potencies of the metal complexes can be arranged as follows: L-Pd > L-Cr > L-Mn > ligand. The sensitivity of the cancer cell lines to these substances was observed in the order of MCF-7 > HepG-2 > HCT-116. These results collectively suggest that the coordination of metal ions to the ligand enhances its anticancer capabilities. The primary factor contributing to the variation in biological activity among these compounds appears to be the alteration of coordination sites, which may influence the formation of more effective hydrogen bonds with the negatively charged DNA of cancer cells due to the metal ions' positive charge [59–62].

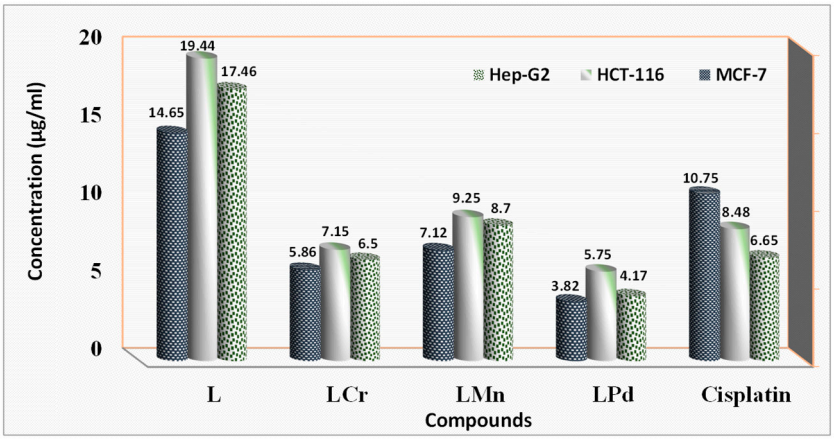


Figure 13. IC_{50} of the ligand, its metal chelates, and the medication Cisplatin versus Hep-G2, HCT-116, and MCF-7 cell lines.

The cytotoxicity assessment of the investigated compounds revealed significant differences in their biocompatibility toward normal human cells. The investigated imine ligand exhibited the highest IC_{50} values, averaging 356.63 and 415.42 μg/μL for human dermal fibroblasts and PBMCs, respectively, indicating excellent biocompatibility and minimal toxicity. In contrast, PdL nanoparticles showed lower cytotoxicity, with IC_{50} values ranging from 218.6 to 263.75 μg/μL, likely due to oxidative stress induced by Pd^{2+} ion release.

When compared with the standard anticancer agent cisplatin, which exhibited IC_{50} values of 192.85 μg/μL for dermal fibroblasts and 205.30 μg/μL for PBMCs, the investigated compounds demonstrated substantially lower toxicity profiles. This stark contrast highlights the potential of investigated imine complexes as safer alternatives for biomedical applications, especially in drug delivery or theranostics, where minimizing off-target toxicity is crucial.

Imine (Schiff base) metal complexes exhibit significant anticancer activity through multiple mechanisms [34,36] (Figure 14). They can interact with DNA by intercalation or covalent bonding, disrupting replication and transcription, ultimately leading to cell death. Additionally, these complexes induce reactive oxygen species (ROS) production, causing oxidative stress and cellular damage. They also inhibit key enzymes such as topoisomerases and proteasomes, preventing cancer cell proliferation. Furthermore, some imine complexes disrupt mitochondrial function, triggering apoptosis through intrinsic pathways. The metal center in these complexes can participate in redox reactions, enhancing cytotoxic effects. Overall, imine metal complexes exert anticancer effects by inducing DNA damage, oxidative stress, enzyme inhibition, and mitochondrial disruption, making them promising candidates for chemotherapy.

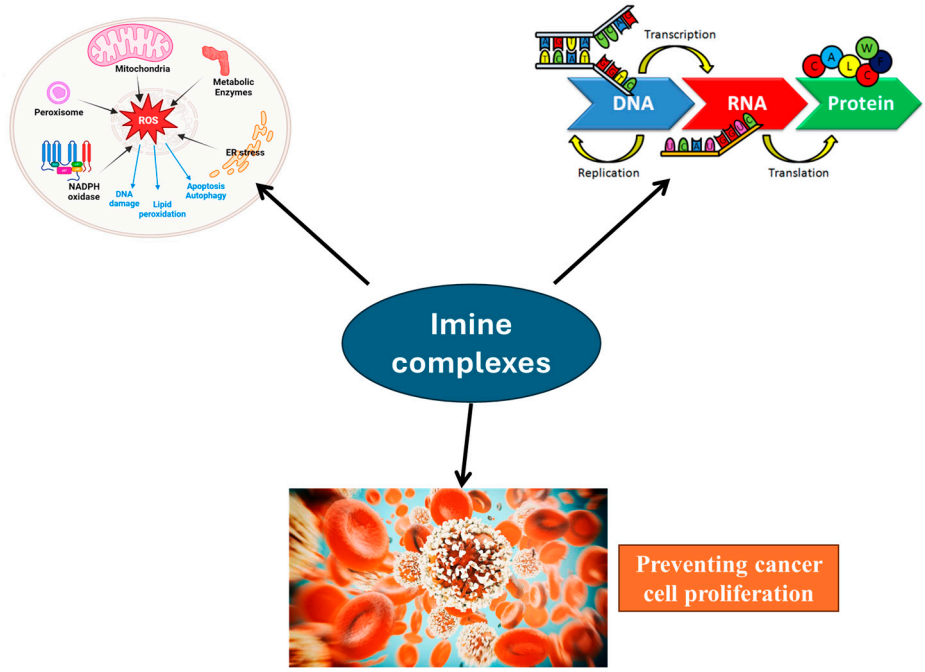


Figure 14. Pathway for anticancer mechanism of the investigated imine complexes. Figure generated using AI-assisted illustration tools for conceptual visualization purposes only.

2.16. Examination of DPPH Radicals Scavenging Efficiency

Oxidative processes mediated by free radicals are substantially implicated in the pathogenesis of various human ailments, including the aging process [63]. The novel synthesized compound, 4-chloro-2-(quinolin-8-yliminomethyl)-phenol, and its corresponding metal complexes were subjected to in vitro antioxidant assays to explore their therapeutic potential. The DPPH free radical scavenging method was employed for these evaluations due to its widespread use and practical advantages. The assay involved preparing solutions with varying concentrations of the ligand and its metal chelates (10, 25, 50, 100, and 150 µg ml^{-1}) to assess their antioxidant efficacy. Ascorbic acid served as a benchmark for comparison purposes. The findings reveal that the metal-bound forms of the ligand generally displayed greater antioxidant capacity than the free ligand itself. Specifically, it was observed that the antioxidant potency of all the complexes escalated in tandem with concentration augmentation. Further analysis demonstrated that the **L-Pd** complex presented the most proficient antioxidant activity, characterized by the lowest IC_{50} value of 15.35 µg/mL, as depicted in Figure 15 and Table S5. Conversely, the **L-Mn** complex exhibited the least antioxidant efficacy among the examined complexes, with an IC_{50} value of 25.60 µg ml^{-1}. This suggests that metal chelation can enhance the antioxidant properties of the ligand, potentially offering a promising avenue for the development of new antioxidant therapies.

The correlation between the prepared imine complexes and their biological activity is influenced by several factors. Firstly, the nanosized form provides a significantly higher surface-area-to-volume ratio, enhancing interactions with biological targets such as enzymes, DNA, and cellular membranes. This leads to improved solubility y and bioavailability, making the complexes more effective in biological systems. Additionally, their reduced size facilitates cellular uptake through mechanisms like endocytosis or passive diffusion, allowing for better penetration and interaction with intracellular targets, which can enhance antibacterial, antifungal, or anticancer activity.

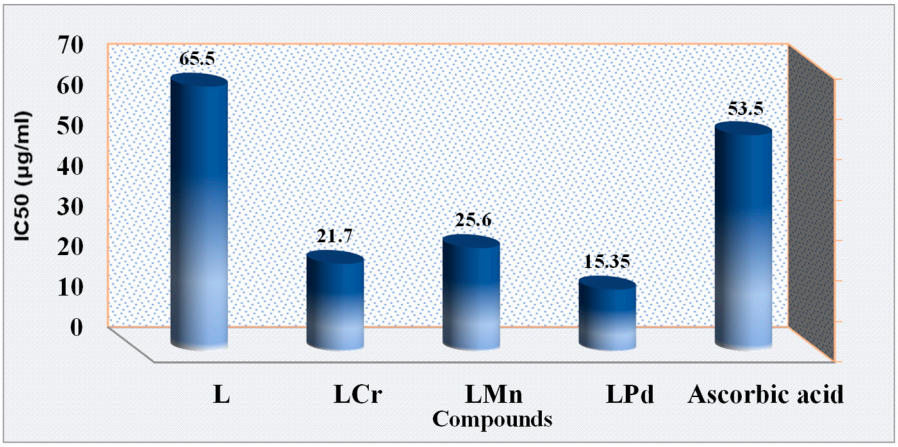


Figure 15. The ligand and its metal complexes inhibit the DPPH radical.

The nanoscale morphology of the solid complexes may influence parameters such as dissolution rate and bioavailability; however, upon dissolution in DMSO, the biologically active species are expected to be discrete metal–ligand molecules. Therefore, docking studies and mechanistic interpretations are based on the molecular form rather than nanoparticle aggregates. Their enhanced chemical and thermal stability prevent premature degradation, allowing for a sustained release of the active compound, which in turn improves therapeutic efficacy while minimizing toxicity. Many of these complexes incorporate metal ions such as Cr, Mn, or Pd, which contribute to biological activity through mechanisms like reactive oxygen species (ROS) generation, enzyme inhibition, or DNA cleavage, leading to potentiated antimicrobial and anticancer effects.

Another key advantage of nanosized imine complexes is their potential for selective targeting. Their surface can be functionalized to improve specificity toward diseased cells, such as cancerous cells, while reducing interactions with healthy cells, thereby minimizing off-target toxicity. This selective targeting, combined with their enhanced bioavailability and stability, makes nanosized imine complexes promising candidates for biomedical applications. Overall, their nanoscale properties significantly enhance their biological activity, making them more efficient and effective compared to their bulk counterparts.

3. Experimental

3.1. Reagents

All chemicals and solvents employed in the research were of analytical purity and utilized directly as obtained, without further purification. These comprised the precursors for the synthesis of imine ligands, namely 8-aminoquinoline and 5-chloro-2-hydroxybenzaldehyde (98%), as well as ethanol (99.9%), acetone (99%), N, N′-dimethylformamide (DMF) (98.5%), and dimethylsulfide (DMSO) (99%), obtained from Sigma-Aldrich, Schnelldorf, Germany. The study involved the use of these solvents without prior distillation. For the preparation of imine metal complexes, the following transition metal salts purchased from Sigma-Aldrich were utilized: $Mn(NO_3)_2{\cdot}4H_2O$ (99%), $Pd(OAc)_2$ (98.5%), and $Cr(NO_3)_3{\cdot}9H_2O$ (98%). These salts were selected for their established role in facilitating the formation of complex compounds and were essential to the experimental procedures conducted.

3.2. Instrumentation

All instrumentation and methods which used in the current investigation are supplied in the Supplementary Materials.

3.3. Synthesis of Tri-Dentate L Imine Ligand

The compound 4-chloro-2-(quinolin-8-yliminomethyl)-phenol (L) was synthesized using a condensation reaction (cf. Scheme 1). The process involved the combination of 8-aminoquinoline (2.88 g, 20 mmol) and 5-chloro-2-hydroxybenzaldehyde (3.13 g, 20 mmol) in a solvent of ethanol, EtOH (25 mL). To facilitate the reaction, the solution was heated to reflux for a duration of three hours. Upon completion of the heating period, the reaction mixture was allowed to cool to room temperature, which promoted the precipitation of a brown solid. The precipitate was isolated through the process of filtration to separate it from the remaining liquid components. Following the separation, the solid was further purified by recrystallization in ethanol, and dried in a desiccator to remove any adsorbed solvent molecules.

L ^{1}H NMR (400 MHz, DMSO-d_6): d (ppm) 13.98 (s, 1H, OH), 9.26 (s, 1H, CH=N), 8.83–8.80 (d, 1H, CH_{arm} adjacent nitrogen of quinoline moiety), 8.61–8.07 (d, *J* = 6.9 Hz 3H, CH_{arm} of pyridine ring in quinoline moiety), 7.90–6.83 (d, *J* = 7.1 Hz 3H, CH_{arm}), 7.42–6.81 (d, *J* = 7.1 2H, CH_{arm} of quinoline moiety). ^{13}C NMR (δ, ppm) in DMSO-d6: 167.30 (CH=N), 163.60 (C-OH), 152.20 (C=N of pyridine ring in quinoline moiety), 140.50 (right carbon adjacent nitrogen tom in quinoline moiety), 138.20 (left carbon adjacent nitrogen tom in quinoline moiety), 134.50 (carbon in para position for nitrogen tom in quinoline moiety), 132.10 (right carbon adjacent chloride atom in phenyl ring), 128.70 (left carbon adjacent chloride atom in phenyl ring), 127.10, 125.50, 124.70, 123.10, 121.10, 120.00, 115.20, 109.50.

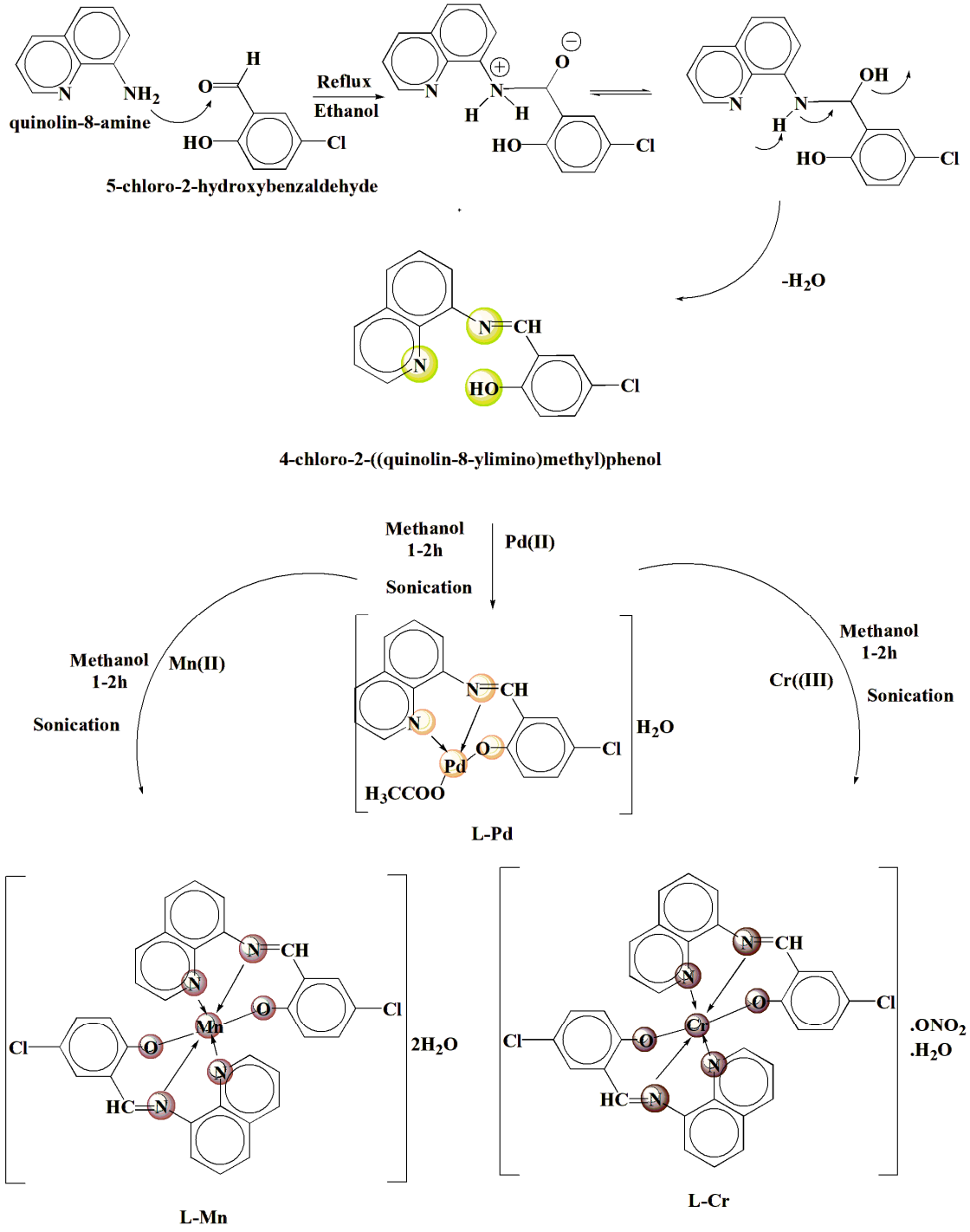
3.4. Sono-Chemical Synthesis of Pd(II), Mn(II), and Cr(III) Complexes with 4-Chloro-2-(Quinolin-8-Yliminomethyl)-Phenol Ligand

Sono-chemical synthesis refers to the use of ultrasonic waves to promote chemical reactions. This method is particularly useful in synthesizing metal complexes, including **Salen metal complexes**, as it enhances reaction rates, improves yields, and leads to better product purity.

A methanolic solution (20 mL) of $Cr(NO_3)_3.9H_2O$ or $Mn(NO_3)_2.4H_2O$ or $Pd(OAc)_2$ (2 mmol) is prepared and added dropwise to a methanolic solution of the ligand (2 mmol) under continuous **ultrasonic irradiation** at 40 kHz. The reaction mixture is subjected to sonication at room temperature for 1–2 h, leading to the formation of the investigated complexes (cf. Scheme 1). The obtained precipitate is filtered, washed with ethanol and ether, and dried under vacuum.

3.5. Estimating the Stoichiometry of Chelates Using Job's and Molar Ratio Methods

The solubility and molar masses of Cr(III), Mn(II), and Pd(II) complexes were scrutinized in this study. Employing Job's continuous variation approach, the researchers examined the stability of these complexes in solution by systematically varying the molar ratios of the metal (M) and ligand (L) species. Following the preparation of these mixtures, the systems were meticulously equilibrated, and the digestibility rate for each specific combination was meticulously noted. The analysis was conducted by monitoring the absorbance of the individual solutions, with the ligand mole fraction ([L]/[L] + [M]) or the molar ratio ([L]/[M]) serving as key parameters to evaluate the stability and molecular weight of the formed complexes [64].



Scheme 1. Diagrammatic approach to the synthesis of the ligand and associated metal complexes.

3.6. Assessment of the Apparent Constant of Complexes

The formation constants (K_f) of the examined chelates have been derived for intensively studied systems, utilizing Job's method in conjunction with spectrophotometric analysis. This technique involves the following equations for different molar ratios:

For a 1:1 molar ratio [37,65],

$$k_f = \frac{\frac{A}{A_M}}{C\left(1 - A/A_m\right)^2} \quad (7)$$

Conversely, for a 1:2 molar ratio,

$$k_f = \frac{\frac{A}{A_M}}{4C^2\left(1 - A/A_m\right)^3} \quad (8)$$

Here, A represents the starting molar concentration of the metal ion, A_M is the maximum transmittance corresponding to the formation of the topmost chelate complex, and C denotes the transmittance at a specific wavelength within the transmittance range.

To evaluate the Gibbs free energy changes (ΔG) associated with these chelate formations, the following equation has been applied:

$$\Delta G = -RT \ln(K_f) \quad (9)$$

where R is the universal gas constant, T is the temperature in Kelvin, and K_f is the formation constant of the chelate. This relationship allows for the determination of the thermodynamic stability of the complexes formed.

3.7. Magnetic Moment Measurements

The assessment of magnetic susceptibility is a highly proficient strategy for examining the structural arrangement of complexes involving transition metals [66]. This process entails the determination of the molar susceptibility of the coordination complex, which is achieved by implementing diamagnetic corrections to account for the presence of other ions or molecules in the sample mixture. This methodology allows for the quantification of the susceptibility of a single paramagnetic metal atom within the material under investigation [67]. Several approaches are available for determining these diamagnetic adjustments; however, one prevalent technique relies on the premises established by Pascal. This approach incorporates specific relationships and equations that facilitate the precise calculation of magnetic susceptibility and the resultant effective magnetic moment.

$$\mu_{eff} = 2.83\sqrt{X_A.T} \quad (10)$$

$$X_A = X_M - (\text{diamagnetic correction}) \quad (11)$$

$$X_M = X_g.M.wt \quad (12)$$

The expression involves several variables: T represents absolute temperature in Kelvin, eff signifies the practical magnetic moment in Bohr Magnetons (B.M), X_g indicates the measured gm magnetic susceptibility, X_M denotes the molar magnetic permeability prior to correction, and X_A symbolizes the molar magnetic permeability following correction

3.8. Spectrophotometric Studies

For the purpose of examining ultraviolet–visible light wavelengths spanning from 200 to 700 nanometers, standard solutions of metal chelate with a concentration of 10^{-3} mol/L were concocted. This was accomplished by meticulously measuring and adding the required volumes of the metal compounds to dimethylformamide, serving as the solvent medium.

3.9. Thermogravimetric Analysis and Kinetic Studies

To evaluate the thermal stability of the complex, thermogravimetric analysis (TGA) was employed to determine the solvent's role within the coordination environment. Additionally, it is imperative to establish the metal content of the mixture. This heating process is governed by kinetics, which allows for the assessment of both kinetic and thermodynamic

properties. For this purpose, the Coats–Redfern method was utilized, as detailed in the literature [68,69].

The kinetic equation used is given by

$$\ln = \left[\frac{g(\alpha)}{T^2}\right] = ln\left(\frac{AR}{\beta E}\right) - \frac{E}{RT} \quad (13)$$

R represents the gas constant, and g(α) is defined differently based on the reaction order, n. When n is not equal to 1, g(α) is expressed as $g(\alpha) = 1 - (1 - \alpha)^{1-n}/1 - n$. Conversely, for n = 1, g(α) simplifies to $g(\alpha) = -\ln(1 - \alpha)$. The correlation coefficient, denoted as r, was computed using the least squares method for a range of n values (n = 1.00, 0.66, 0.51, and n = 0.33). The relationship between ln [$g(\alpha)/T^2$] and 1/T was graphically presented, and the reaction order was selected as the n-value that yielded the most accurate fit ($r \approx 1$). The intercept provides the pre-exponential factor (A), and the slope offers the activation energy (Ea)/R. Thermodynamic parameters were also derived from this approach, analogous to the determination of A and E [70].

3.10. DFT and Docking Studies

3.10.1. DFT Calculations

Quantum mechanical atomistic simulations were conducted using DFT perspective to analyze various properties of L, L-Pd, L-Mn, and L-Cr compounds. These computations were carried out with the Gaussian 09W software [71], while molecular structures were visualized using GaussView 6.0. Optimization was achieved through the B3LYP hybrid functional, employing the 6-311g (d,p) basis set for lighter atoms and LANL2DZ for heavier ones. This approach facilitated the determination of molecular orbital structures and electrostatic potential surface maps. Additionally, the HOMO and LUMO energy levels, along with the energy gap (E_{gap}), were calculated for both the ligand and its metal complexes. Finally, the quantum reactivity of the studied compounds was assessed based on their molecular orbital energies.

3.10.2. Molecular Docking Approaches

The possible anticancer, antimicrobial, and antifungal effects of the L, L-Pd, L-Mn, and L-Cr compounds were investigated using an in silico docking approach to validate their experimentally observed biological activities. To acquire the initial crystallographic structures of 3HB5 [72]—a breast cancer protein (used for anticancer activity); 4EWP [73]—*Micrococcus luteus* (used for antimicrobial activity); and 5V5Z [74]—*Candida albicans* (used for antifungal activity), a thorough search was conducted in the Protein Data Bank (https://www.rcsb.org/, accessed on 2 June 2025). The ligand and its optimized complexes, obtained from DFT, were converted into PDB format through the GaussView 6.0 program and used as ligands for docking modeling. Molecular docking was performed using AutoDock Tools 1.5.6 in conjunction with Autogrid 4 and AutoDock 4.2 [75]. This process utilized the Lamarckian genetic algorithm (LGA) to identify the potential binding site and determine the optimal orientation of the ligand. For the initial preparation of the macromolecular structure, hydrogen atoms were added, and Kollman charges were appropriately assigned [76]. Furthermore, all water molecules, ligands, and non-essential components were removed from the protein structures [73]. Grid boxes were defined with dimensions of 80 × 90 × 90 Å for 3HB5, 96 × 86 × 96 Å for 4EWP, and 90 × 100 × 100 Å for 5V5Z, with a spacing of 0.375 Å. Ligand poses were extracted using the Chimera package [77] and subsequently analyzed for interaction diagrams using the Discovery Studio Visualizer 4.1 program.

3.11. Biological Evaluate

3.11.1. Antibacterial Activity

The in vitro biological properties of the ligand 4-chloro-2-(quinolin-8-yliminomethyl)-phenol and its complexes were scrutinized in a study to evaluate their efficacy against a range of bacterial strains, including *Micrococcus luteus* (Gram-positive), *Escherichia coli* (Gram-negative), and *Serratia marcescens* (Gram-negative). The antimicrobial activity was assessed using the well diffusion technique on nutrient agar plates [78]. Additionally, the antifungal potency of these substances was explored against diverse fungal species such as *Fusarium oxysporum*, *Geotrichum candidum*, and *Aspergillus flavus*, employing potato dextrose agar as the growth medium. To prepare the compounds for testing, they were dissolved in dimethyl sulfoxide (DMSO) to achieve concentrations of 10 mg/mL and 20 mg/mL. The experimental setup involved creating wells on the agar plates that had been previously inoculated with the target microorganisms [79,80]. These wells were then filled with the test solutions using a micropipette. For control purposes, some wells contained only DMSO, which served as the negative control, while others contained established antimicrobial agents like Ofloxacin for bacteria and fluconazole for fungi as positive controls. The plates were then incubated at optimal temperatures for the respective microbial groups: 24 h at 37 °C for bacteria and 72 h at 35 °C for fungi. Following the incubation period, the zone of inhibition surrounding the wells was measured using a specialized zone reader (Hi Antibiotic zone scale) to determine the compounds' inhibitory capabilities against the test microbes. It is noteworthy that the solvent DMSO, when used by itself, did not exhibit any antimicrobial activity, ensuring that the observed effects were solely attributed to the ligand and its complexes. The experiment was meticulously conducted with three replicates for each substance to ensure the reliability of the results.

3.11.2. Anticancer Evaluation of Ligand and Its Metal Complexes

The study utilized an ELISA microplate reader (Model Σ960 from Meter Tech, Taipei, Taiwan), which operates with a wavelength of 564 nm to evaluate the effects of the compounds on Hep-G2 (hepatocellular carcinoma, human liver cancer cell line) was obtained from the American Type Culture Collection (ATCC, Manassas, VA, USA), MCF-7 (human breast adenocarcinoma cell line) was purchased from ATCC (Manassas, VA, USA), and HCT-116 (human colorectal carcinoma cell line) was also purchased from ATCC (Manassas, VA, USA). The cellular analysis commenced with the distribution of the cells at a density of 10,000 cells per well in a 96-well plate, allowing them to adhere for 24 h at 37 °C. Afterward, the cells were subjected to different concentrations of the compounds, dissolved in DMSO (0, 1, 2.5, 5, and 10 μM), for a 48 h incubation period within a 5% CO_2 controlled environment at the same temperature. Post-incubation, the plate was processed for fixation and staining with sulfo-rhodamine B. Unwanted stain residues were removed through acetic acid washes, and the plate was treated with Tris-EDTA buffer. The optical density of the stained cells, which correlates with cell viability, was measured by the ELISA reader. The IC_{50} value, indicating the compounds' efficacy, was determined following standard procedures outlined in the literature [81–84].

$$\text{Inhibition concentration (IC) \%} = (\text{Control O.D} - \text{Ligand O.D}) \times 100/\text{Control O.D} \quad (14)$$

3.11.3. Assessment of Antioxidant Activity Using DPPH Radical Scavenging Assay

The investigation into the antioxidant characteristics of the molecules in question was performed via an assessment of their capacity to scavenge DPPH (1,1-diphenyl-2-picrylhydrazyl) free radicals, adhering to the methodological guidelines established [85]. This methodology is a prevalent technique for evaluating the antioxidative potential of

substances. It is predicated on the interaction between the antioxidants and the stable DPPH free radical, which results in a decrease in optical density and a transformation in color from purple to yellow. This change occurs as a consequence of the antioxidants' capability to neutralize the free radicals. The experimental procedure entailed combining 2.0 mL of the chelates under study with 6.0 mL of the DPPH solution. Notably, the chelates were omitted from the control and blank samples. These solutions were then placed in a darkened setting and allowed to incubate for a duration of 0.5 h at a constant temperature of 25 degrees Celsius. Upon completion of the incubation period, spectrophotometric analysis of the transmittance was conducted at a wavelength of 519 nm, which is particularly relevant for monitoring the DPPH reaction's progress. The absorbance of the samples was determined by comparing them to both blank and reference solutions. The calculation of the IC_{50}, which represents the concentration at which the chelates exerted a 50% inhibition of DPPH free radicals, was executed using the appropriate formula:

$$\text{Scavenging activity}(\%) = {}^{A_0 - A_t}\Big/_{A_0} \times 100 \quad (15)$$

where A_0 represents the initial absorbance of the blank (standard) control at time t = 0, and A_t is the absorbance at the end of the reaction. This approach is effective in quantifying the antioxidant effectiveness of the molecules. The assay involved a serial dilution to expose each sample to varying concentrations, and all experiments were triplicated to ensure the reliability of the data [85].

4. Conclusions

Novel nanosized Cr(III), Mn(II), and Pd(II) complexes incorporating the chloro-2-(quinolin-8-yliminomethyl)-phenol imine ligand were synthesized and characterized via different physicochemical and spectroscopic tools. The analytical outcomes indicate that complexes formed with Cr(III) and Mn(II) adhere to a 1:2 metal-to-ligand ratio, whereas the Pd(II) complex has a 1:1 stoichiometry. Conductivity studies revealed that the **L-manganese** and **L-palladium** systems behave as non-electrolytes, whereas the **L-chromium** complex exhibits mono-electrolyte properties due to its elevated conductivity. The ligand's interaction with metal ions is established through the nitrogen atom of the quinoline ring, the oxygen atom of the hydroxyl group, and the nitrogen atom in the azomethine bond. Thermal analysis, including thermogravimetric data, elucidated the degradation patterns of the synthesized complexes, which assisted in their characterization. The complexes' distinct geometrical structures were inferred from the analytical and spectral data: Cr(III) and Mn(II) complexes adopt a high-spin octahedral geometry, while the Pd(II) complex assumes a square-planar conformation. These structural predictions were substantiated by theoretical computations, reinforcing the study's foundational understanding. Biological assessments unveiled significant antifungal and antibacterial properties for the palladium-integrated complex, **L-Pd**, which showcased substantial inhibitory action across a diverse range of microbial strains. The antioxidant potential of the synthesized compounds was evaluated by DPPH assays, showcasing moderate-to-excellent activities in comparison to ascorbic acid, with particular effectiveness against DPPH radicals. The biomedical evaluation of these complexes highlighted their anticancer capabilities, with the palladium complex, **L-Pd**, displaying noteworthy cytotoxicity against three separate cancer cell lines: HCT-116 (colorectal), MCF-7 (breast), and HepG-2 (liver). The most pronounced effect was observed against MCF-7 cells, hinting at a potential breakthrough in the development of antineoplastic agents. This enhanced activity of the L-Pd complex may be attributed to the square-planar geometry of Pd(II), which facilitates stronger interactions with biological targets such as DNA and microbial enzymes. Additionally, the Pd(II) center may form more stable complexes with biomolecules, improving cellular uptake

and bioavailability. These factors likely contribute to the observed superior antifungal, antibacterial, and anticancer performance of the L–Pd complex.

Supplementary Materials: The following supporting information can be downloaded at: https://www.mdpi.com/article/10.3390/inorganics13080271/s1, Figure S1: IR spectra of ligand(L) and its metal complexes; Figure S2: ^{1}H-NMR spectra of ligand (L); Figure S3: ^{13}C-NMR spectra of ligand (L); Figure S4: TGA -DTGA curves for the prepared complexes; Figure S5: Molar ratio plots for the prepared complexes in DMF; Table S1: Electronic Spectra of the ligand (L) and its metal complexes; Table S2: Antibacterial activity inhibition zone of the prepared compounds against the selected strains of bacteria; Table S3: Antifungal activity inhibition zone of the prepared compounds against the selected strains of fungi; Table S4: Cytotoxic activity (IC_{50}) of the prepared compounds against Colon carcinoma cells, (HCT-116 cell line), hepatic cellular carcinoma cells, (HepG-2), breast carcinoma cells (MCF-7) and norma cells (human dermal fibroblasts and PBMCs) for (L) ligand and its metal chelates; Table S5: Antioxidant activity of the investigated compounds.

Funding: This research was funded by Taif University, Saudi Arabia, through project number TU-DSPP-2024-216.

Data Availability Statement: The data that support the findings of this study are available from the corresponding author upon reasonable request.

Acknowledgments: The authors extend their appreciation to Taif University, Saudi Arabia, for supporting this work through project number TU-DSPP-2024-216.

Conflicts of Interest: The author declares that they have no known competing financial interests or personal relationships that could have appeared to influence the work reported in this paper.

References

1. Gogoi, H.P.; Barman, P. Salophen type ONNO donor Schiff base complexes: Synthesis, characterization, bioactivity, computational, and molecular docking investigation. *Inorg. Chim. Acta* **2023**, *556*, 121668. [CrossRef]
2. Al-Farraj, E.S.; Alharbi, S.K.; Feizi-Dehnayebi, M.; Asghar, B.H.; Alahmadi, N.; Eskander, T.N.A.; Alghamdi, M.A.; Abu-Dief, A.M. Molecular, Stochiometric, Stability and Biological Investigations of Novel Multifunctional Salen Metal Chelates: From Synthesis to Therapeutic Potential Supported by Theoretical Approaches. *Appl. Organomet. Chem.* **2025**, *39*, e70273. [CrossRef]
3. El-Kasaby, R.A.; Al-Farraj, E.S.; Abdou, A.; Abu-Dief, A.M. Synthesis, spectral analysis, physicochemical investigation and biomedical potential of some novel Cu(II), Ru(III) and VO(II) complexes with anthraquinone-based Schiff base supported by DFT and molecular docking insights. *J. Mol. Struct.* **2025**, *1345*, 143010. [CrossRef]
4. Abdel-Rahman, L.H.; Abu-Dief, A.M.; Abdel-Mawgoud Azza, A.H. Novel Di-and Tri-azomethine compounds as chemo sensors for the detection of various metal ions. *Int. J. Nano Chem.* **2019**, *5*, 1–17.
5. Vernekar, B.K.; Sawant, P.S. Interaction of metal ions with Schiff bases having N_2O_2 donor sites: Perspectives on synthesis, structural features, and applications. *Results Chem.* **2023**, *6*, 101039. [CrossRef]
6. Bulatov, E.; Sayarova, R.; Mingaleeva, R.; Miftakhova, R.; Gomzikova, M.; Ignatyev, Y.; Petukhov, A.; Davidovich, P.; Rizvanov, A.; Barlev, N.A. Isatin-Schiff base-copper (II) complex induces cell death in p53-positive tumors. *Cell Death Discov.* **2018**, *4*, 103. [CrossRef]
7. Hosny, S.; Shehata, M.R.; Aly, S.A.; Alsehli, A.H.; Salaheldeen, M.; Abu-Dief, A.M.; Abu-El-Wafa, S.M. Synergistic broad-spectrum bioactivity of some multifunctional novel Anil metal chelates: Design, synthesise, nonlinear optical properties, and biomedical applications supported by DFT and molecular docking insights. *J. Mol. Struct.* **2025**, *1339*, 142390. [CrossRef]
8. Hosny, S.; Shehata, M.R.; Aly, S.A.; Alsehli, A.H.; Salaheldeen, M.; Abu-Dief, A.M.; Abu-El-Wafa, S.M. Designing of novel nano-sized coordination compounds based on Spinacia oleracea extract: Synthesis, structural characterization, molecular docking, computational calculations, and biomedical applications. *Inorg. Chem. Commun.* **2024**, *160*, 111994. [CrossRef]
9. El-Lateef, H.M.A.; Khalaf, M.M.; Shehata, M.R.; Abu-Dief, A.M. Fabrication, DFT Calculation, and Molecular Docking of Two Fe(III) Imine Chelates as Anti-COVID-19 and Pharmaceutical Drug Candidate. *Int. J. Mol. Sci.* **2022**, *23*, 3994. [CrossRef]
10. Abu-Dief, A.M.; Said, M.A.; Elhady, O.; Al-Abdulkarim, H.A.; Alzahrani, S.; Eskander, T.N.A.; El-Remaily, M.A.E.A.A.A. Innovation of Fe(III), Ni(II), and Pd(II) complexes derived from benzothiazole imidazolidin-4-ol ligand: Geometrical elucidation, theoretical calculation, and pharmaceutical studies. *Appl. Organomet. Chem.* **2023**, *37*, e7162. [CrossRef]
11. Gupta, K.C.; Sutar, A.K. Catalytic activities of Schiff base transition metal complexes. *Coord. Chem. Rev.* **2008**, *252*, 1420–1450. [CrossRef]

12. Shaaban, S.; Yousef, T.A.; Al-Janabi, A.S.; Alammar, T.; Alaasar, M.; Shalabi, K.; Al-Karmalawy, A.A.; Ferjani, H.; Al-Dakhil, A.; Abu-Dief, A.M. Zn(II), Cu(II), and Fe(III) complexes of 2-(((4-(Methylselanyl) phenyl)imino)methyl)phenol: Synthesis, characterization, and multidisciplinary investigations. *Polyhedron* **2025**, *279*, 117652. [CrossRef]
13. Al-Ghamdi, K.; Alharas, M.M.; Abdel-Latif, S.A.; Alhashmialameer, D.; Al-Farraj, E.S.; Almalki, M.A.; El-Khatib, R.M.; Abu-Dief, A.M. Selective Novel Metal-Coordinated Biomedical Agents Encompassing Tetradentate Salen Ligand: Structural Elucidation, DFT Calculation, Cytotoxic, and Antioxidant Activities Supported by Molecular Docking Approach. *Appl. Organomet. Chem.* **2025**, *39*, e7991. [CrossRef]
14. Al-Abdulkarim, H.A.; El-khatib, R.M.; Aljohani, F.S.; Mahran, A.; Alharbi, A.; Mersal, G.A.; El-Metwaly, N.M.; Abu-Dief, A.M. Optimization for synthesized quinoline-based Cr^{3+}, VO^{2+}, Zn^{2+} and Pd^{2+} complexes: DNA interaction, biological assay and in-silico treatments for verification. *J. Mol. Liq.* **2021**, *339*, 116797. [CrossRef]
15. Abu-Dief, A.M.; Shehata, M.R.; Hassan, A.E.; Altayeb, B.M.; Aljohani, F.S.; Barnawi, I.O.; Abo-Dief, H.M.; Ragab, M.S. Tailoring of novel water soluble Pd(II), Cu(II), Fe(III) and VO(II) chelates based on 4-[(5-bromo-2-hydroxy-benzylidene)-amino]-benzenesulfonate ligand: Synthesis, spectral investigations, DNA interaction and pharmaceutical applications supported by molecular docking approach. *J. Mol. Struct.* **2025**, *1334*, 141780.
16. Al-Fakeh, M.S.; Alsikhan, M.A.; Alnawmasi, J.S. Physico-chemical study of Mn(II), Co(II), Cu(II), Cr(III), and Pd(II) complexes with schiff-base and aminopyrimidyl derivatives and anti-cancer, antioxidant, antimicrobial applications. *Molecules* **2023**, *28*, 2555. [CrossRef]
17. Suslick, K.S. Sonochemistry. *Science* **1990**, *247*, 1439–1445. [CrossRef] [PubMed]
18. Mason, T.J.; Peters, D. *Practical Sonochemistry: Power Ultrasound Uses and Applications*; Woodhead Publishing: Cambridge, UK, 2002.
19. Abu-Dief, A.M.; Said, M.A.; Elhady, O.; Alahmadi, N.; Alzahrani, S.; Eskander, T.N.A.; Ali, M.A.E.A.A. Designing of some novel Pd(II), Ni(II) and Fe(III) complexes: Synthesis, structural elucidation, biomedical applications, DFT and docking approaches against COVID-19. *Inorg. Chem. Commun.* **2023**, *155*, 110955. [CrossRef]
20. Gozdas, S.; Kose, M.; Mckee, V.; Elmastas, M.; Demirtas, I.; Kurtoglu, M. Crystal structures, electronic spectra and anticancer properties of new azo-azomethines and their nickel(II) and copper(II) chelates. *J. Mol. Struct.* **2024**, *1304*, 137691. [CrossRef]
21. Shaaban, S.; Abdullah, K.T.; Shalabi, K.; Yousef, T.A.; Al Duaij, O.K.; Alsulaim, G.M.; Althikrallah, H.A.; Alaasar, M.; Al-Janabi, A.S.; Abu-Dief, A.M. Synthesis, structural characterization, anticancer, antimicrobial, antioxidant, and computational assessments of zinc(II), iron(II), and copper(II) chelates derived from selenated Schiff base. *Appl. Organomet. Chem.* **2024**, *38*, e7712. [CrossRef]
22. Khalaf, M.M.; Abd El-Lateef, H.M.; Taha, A.A.; Abdou, A. Binuclear Fe(II) and Cu(II) complexes with 2-(pyridin-2-yl)-1H-benzimidazole and 4,4′-bipyridine: Synthesis, characterization, DFT insights, broad-spectrum bioactivity and docking study. *Inorganica Chim. Acta* **2025**, *577*, 122505. [CrossRef]
23. Abdel-Rhman, M.H.; Motawea, R.; Belal, A.; Hosny, N.M. Spectral, structural and cytotoxicity studies on the newly synthesized n'^1, n'^3-diisonicotinoylmalonohydrazide and some of its bivalent metal complexes. *J. Mol. Struct.* **2022**, *1251*, 131960. [CrossRef]
24. Hosny, N.M.; Ibrahim, O.A.; Belal, A.; Hussien, M.A.; Abdel-Rhman, M.H. Synthesis, characterization, DFT, cytotoxicity evaluation and molecular docking of a new carbothioamide ligand and its coordination compounds. *Results Chem.* **2023**, *5*, 100776. [CrossRef]
25. Ali, I.; Wani, W.A.; Saleem, K. Empirical formulae to molecular structures of metal complexes by molar conductance. *Synth. React. Inorg. Met.-Org. Nano-Met. Chem.* **2013**, *43*, 1162–1170. [CrossRef]
26. Khalaf, M.M.; Abd El-Lateef, H.M.; Gouda, M.; Sayed, F.N.; Mohamed, G.G.; Abu-Dief, A.M. Design, structural inspection and bio-medicinal applications of some novel imine metal complexes based on acetylferrocene. *Materials* **2022**, *15*, 4842. [CrossRef] [PubMed]
27. Ali, O.A. Characterization, thermal and fluorescence study of Mn(II) and Pd(II) Schiff base complexes. *J. Therm. Anal. Calorim.* **2017**, *128*, 1579–1590. [CrossRef]
28. Soliman, M.H.; Mohamed, G.G. Cr(III), Mn(II), Fe(III), Co(II), Ni(II), Cu(II) and Zn(II) new complexes of 5-aminosalicylic acid: Spectroscopic, thermal characterization and biological activity studies. *Spectrochim. Acta Part A Mol. Biomol. Spectrosc.* **2013**, *107*, 8–15. [CrossRef]
29. Zare, N.; Zabardasti, A. A new nano-sized mononuclear Cu (II) complex with N,N-donor Schiff base ligands: Sonochemical synthesis, characterization, molecular modeling and biological activity. *Appl. Organomet. Chem.* **2019**, *33*, e4687. [CrossRef]
30. Al-Hazmi, G.A.; Abou-Melha, K.S.; Althagafi, I.; El-Metwaly, N.; Shaaban, F.; Abdul Galil, M.S.; El-Bindary, A.A. Synthesis and structural characterization of oxovanadium(IV) complexes of dimedone derivatives. *Appl. Organomet. Chem.* **2020**, *34*, e5672. [CrossRef]
31. Refat, M.S.; Altalhi, T.; Bakare, S.B.; Al-Hazmi, G.H.; Alam, K. New Cr(III), Mn(II), Fe(III), Co(II), Ni(II), Zn(II), Cd(II), and Hg(II) gibberellate complexes: Synthesis, structure, and inhibitory activity against COVID-19 protease. *Russ. J. Gen. Chem.* **2021**, *91*, 890–896. [CrossRef] [PubMed]

32. El-Remaily, M.A.E.A.A.A.; Eskander, T.N.A.; Elhady, O.; Alhashmialameer, D.; Alsehli, M.; Kamel, M.S.; Feizi-Dehnayebi, M.; Abu-Dief, A.M. A comparative study for the efficiency of Pd(II) and Fe(III) complexes as efficient catalysts for synthesis of dihydro-7H-5-thia-hexaaza-s-indacen-6-one derivatives supported with DFT approach. *Appl. Organomet. Chem.* **2024**, *38*, e7653. [CrossRef]
33. Abdel-Rahman, L.H.; Abu-Dief, A.M.; Aboelez, M.O.; Abdel-Mawgoud, A.A.H. DNA interaction, antimicrobial, anticancer activities and molecular docking study of some new VO(II), Cr(III), Mn(II) and Ni(II) mononuclear chelates encompassing quaridentate imine ligand. *J. Photochem. Photobiol. B Biol.* **2017**, *170*, 271–285. [CrossRef] [PubMed]
34. Yousef, T.A.; El-Reash, G.A.; El-Gammal, O.A.; Bedier, R.A. Co(II), Cu(II), Cd(II), Fe(III) and U(VI) complexes containing a NSNO donor ligand: Synthesis, characterization, optical band gap, in vitro antimicrobial and DNA cleavage studies. *J. Mol. Struct.* **2012**, *1029*, 149–160. [CrossRef]
35. Abdel-Rahman, L.H.; Abu-Dief, A.M.; Moustafa, H.; Hamdan, S.K. Ni(II) and Cu(II) complexes with ONNO asymmetric tetradentate Schiff base ligand: Synthesis, spectroscopic characterization, theoretical calculations, DNA interaction and antimicrobial studies. *Appl. Organomet. Chem.* **2017**, *31*, e3555. [CrossRef]
36. Aljohani, E.T.; Shehata, M.R.; Alkhatib, F.; Alzahrani, S.O.; Abu-Dief, A.M. Development and structure elucidation of new VO^{2+}, Mn^{2+}, Zn^{2+}, and Pd^{2+} complexes based on azomethine ferrocenyl ligand: DNA interaction, antimicrobial, antioxidant, anticancer activities, and molecular docking. *Appl. Organomet. Chem.* **2021**, *35*, e6154. [CrossRef]
37. Munde, A.S.; Jagdale, A.N.; Jadhav, S.M.; Chondhekar, T.K. Synthesis, characterization and thermal study of some transition metal complexes of an asymmetrical tetradentate Schiff base ligand. *J. Serbian Chem. Soc.* **2010**, *75*, 349–359. [CrossRef]
38. El-Remaily, M.A.E.A.A.A.; Elhady, O.; Eskander, T.N.A.; Mohamed, S.K.; Abu-Dief, A.M. Development of novel guanidine iron (III) complexes as a powerful catalyst for the synthesis of tetrazolo [1,5-a] pyrimidine by green protocol. *Sohag J. Sci.* **2024**, *9*, 7–15. [CrossRef]
39. Abu-Dief, A.M.; Said, M.A.; Elhady, O.; Alzahrani, S.; Aljohani, F.S.; Eskander, T.N.A.; Ali, M.A.E.A.A. Design, structural inspection of some new metal chelates based on benzothiazol-pyrimidin-2-ylidene ligand: Biomedical studies and molecular docking approach. *Inorg. Chem. Commun.* **2023**, *158*, 111587. [CrossRef]
40. Abu-Dief, A.M.; Feizi-Dehnayebi, M.; Nafady, A.; Almalki, M.A.; Kassem, A.M.; Abu Al-Ola, K.A.; Altayeb, B.M.; Abdel-Rahman, L.H. Fabrication, structural inspection, stability studies in solution and DFT calculations of some novel complexes drived from 4-(Benzothiazol-2-yliminomethyl)-phenol ligand: Pharmaceutical applications supported by molecular docking approach. *J. Mol. Struct.* **2025**, *1328*, 141284. [CrossRef]
41. Kazachenko, A.S.; Issaoui, N.; Holikulov, U.; Al-Dossary, O.M.; Ponomarev, I.S.; Kazachenko, A.S.; Akman, F.; Bousiakou, L.G. Noncovalent interactions in *N*-methylurea crystalline hydrates. *Z. Phys. Chem.* **2024**, *238*, 89–114. [CrossRef]
42. Akman, F.; Demirpolat, A.; Kazachenko, A.S.; Kazachenko, A.S.; Issaoui, N.; Al-Dossary, O. Molecular structure, electronic properties, reactivity (ELF, LOL, and Fukui), and NCI-RDG studies of the binary mixture of water and essential oil of Phlomis bruguieri. *Molecules* **2023**, *28*, 2684. [CrossRef]
43. Dehghani, N.; Ziarani, G.M.; Feizi-Dehnayebi, M.; Mirhosseyni, M.; Badiei, A. Synthesis and theoretical investigation of a new Hg^{2+} chemosensor based nanomagnetic particle (Fe_3O_4@SiO_2@ Pr-NCIM). *Mater. Res. Bull.* **2025**, *183*, 113200. [CrossRef]
44. Mohammadi Ziarani, G.; Rezakhani, M.; Feizi-Dehnayebi, M.; Nikolova, S. Fumed-Si-Pr-Ald-Barb as a fluorescent chemosensor for the Hg^{2+} detection and $Cr_2O_7^{2-}$ ions: A combined experimental and computational perspective. *Molecules* **2024**, *29*, 4825. [CrossRef]
45. Mohammadi Ziarani, G.; Ebrahimi, D.; Feizi-Dehnayebi, M.; Badiei, A.; Abu-Dief, A.M. Tailored Silica-Based Sensors (SBA-Pr-Ald-MA) for Efficient Detection of Iron (III) Ions: A Comprehensive Theoretical and Experimental Viewpoint. *Appl. Organomet. Chem.* **2025**, *39*, e7917. [CrossRef]
46. Zamiran, F.; Mohammadi Ziarani, G.; Feizi-Dehnayebi, M.; Mirhosseyni, M.; Badiei, A.; Abu-Dief, A.M. Design, Preparation, Characterization, Density Functional Theory, and HOMO-LUMO Perspective of Fe_3O_4@SiO_2-Pr-NH-IC as a New Nanomagnetic Chemosensor. *Appl. Organomet. Chem.* **2025**, *39*, e7998. [CrossRef]
47. Gungor, O.; Gul, A.; Comertpay, S.; McKee, V.; Yalcinkaya, O.B.; Kose, M. Copper(II) and Zinc(II) complexes of new water-soluble Schiff base ligands and their antiproliferative properties towards mesothelioma cell line. *J. Photochem. Photobiol. A Chem.* **2025**, *459*, 116049. [CrossRef]
48. Canakdag, M.; Feizi-Dehnayebi, M.; Kundu, S.; Sahin, D.; İlhan, İ.Ö.; Alhag, S.K.; Al-Shuraym, L.A.; Akkoc, S. Comprehensive evaluation of purine analogues: Cytotoxic and antioxidant activities, enzyme inhibition, DFT insights, and molecular docking analysis. *J. Mol. Struct.* **2025**, *1323*, 140798. [CrossRef]
49. El-Remaily, M.A.E.A.A.A.; El-Dabea, T.; El-Khatib, R.M.; Abdou, A.; El Hamd, M.A.; Abu-Dief, A.M. Efficiency and development of guanidine chelate catalysts for rapid and green synthesis of 7-amino-4,5-dihydro-tetrazolo [1,5-a] pyrimidine-6-carbonitrile derivatives supported by density functional theory (DFT) studies. *Appl. Organomet. Chem.* **2023**, *37*, e7262. [CrossRef]
50. Pérez, P.; Domingo, L.R.; Aizman, A.; Contreras, R. The electrophilicity index in organic chemistry. *Theor. Comput. Chem.* **2007**, *19*, 139–201.

51. Raman, N.; Raja, J.D. Synthesis, structural characterization and antibacterial studies of some biosensitive mixed ligand copper (II) complexes. *Indian J. Chem. Sect. A* **2007**, *46*, 1611–1614.
52. Abdel-Rahman, L.H.; Abdelhamid, A.A.; Abu-Dief, A.M.; Shehata, M.R.; Bakheet, M.A. Facile synthesis, X-ray structure of new multi-substituted aryl imidazole ligand, biological screening and DNA binding of its Cr(III), Fe(III) and Cu(II) coordination compounds as potential antibiotic and anticancer drugs. *J. Mol. Struct.* **2020**, *1200*, 127034. [CrossRef]
53. Epand, R.M.; Walker, C.; Epand, R.F.; Magarvey, N.A. Molecular mechanisms of membrane targeting antibiotics. *Biochim. Biophys. Acta (BBA)-Biomembr.* **2016**, *1858*, 980–987. [CrossRef]
54. Ansel, H.C.; Norred, W.P.; Roth, I.L. Antimicrobial activity of dimethyl sulfoxide against *Escherichia coli*, *Pseudomonas aeruginosa*, and *Bacillus megaterium*. *J. Pharm. Sci.* **1969**, *58*, 836–839. [CrossRef] [PubMed]
55. Tweedy, B.G. Possible mechanism for reduction of elemental sulfur by *Monilinia fructicola*. *Phytopathology* **1964**, *54*, 910.
56. Abu-Dief, A.M.; El-Metwaly, N.M.; Alzahrani, S.O.; Alkhatib, F.; Abualnaja, M.M.; El-Dabea, T.; Ali, M.A.E.A.A. Synthesis and characterization of Fe(III), Pd(II) and Cu(II)-thiazole complexes; DFT, pharmacophore modeling, in-vitro assay and DNA binding studies. *J. Mol. Liq.* **2021**, *326*, 115277. [CrossRef]
57. Sindhu, Y.; Athira, C.J.; Sujamol, M.S.; Joseyphus, R.S.; Mohanan, K. Synthesis, characterization, DNA cleavage, and antimicrobial studies of some transition metal complexes with a novel Schiff base derived from 2-aminopyrimidine. *Synth. React. Inorg. Met.-Org. Nano-Met. Chem.* **2013**, *43*, 226–236. [CrossRef]
58. Mohamed, G.G.; Soliman, M.H. Synthesis, spectroscopic and thermal characterization of sulpiride complexes of iron, manganese, copper, cobalt, nickel, and zinc salts. Antibacterial and antifungal activity. *Spectrochim. Acta Part A Mol. Biomol. Spectrosc.* **2010**, *76*, 341–347. [CrossRef]
59. Aljohani, F.S.; Abu-Dief, A.M.; El-Khatib, R.M.; Al-Abdulkarim, H.A.; Alharbi, A.; Mahran, A.; Khalifa, M.E.; El-Metwaly, N.M. Structural inspection for novel Pd(II), VO(II), Zn(II) and Cr(III)-azomethine metal chelates: DNA interaction, biological screening and theoretical treatments. *J. Mol. Struct.* **2021**, *1246*, 131139. [CrossRef]
60. El-Wakiel, N.A. Synthesis and characterization of azo sulfaguanidine complexes and their application for corrosion inhibition of silicate glass. *Appl. Organomet. Chem.* **2016**, *30*, 664–673. [CrossRef]
61. Abdel-Rahman, L.H.; Adam, M.S.S.; Abu-Dief, A.M.; Moustafa, H.; Basha, M.T.; Aboraia, A.S.; Al-Farhan, B.S.; Ahmed, H.E.S. Synthesis, theoretical investigations, biocidal screening, DNA binding, in vitro cytotoxicity and molecular docking of novel Cu(II), Pd(II) and Ag(I) complexes of chlorobenzylidene Schiff base: Promising antibiotic and anticancer agents. *Appl. Organomet. Chem.* **2018**, *32*, e4527. [CrossRef]
62. Abdel-Rahman, L.H.; Abu-Dief, A.M.; Shehata, M.R.; Atlam, F.M.; Abdel-Mawgoud, A.A.H. Some new Ag(I), VO(II) and Pd(II) chelates incorporating tridentate imine ligand: Design, synthesis, structure elucidation, density functional theory calculations for DNA interaction, antimicrobial and anticancer activities and molecular docking studies. *Appl. Organomet. Chem.* **2019**, *33*, e4699. [CrossRef]
63. Gaetke, L.M.; Chow, C.K. Copper toxicity, oxidative stress, and antioxidant nutrients. *Toxicology* **2003**, *189*, 147–163. [CrossRef]
64. El-Remaily, M.A.E.A.A.A.; Elhady, O.; Alzubi, M.S.H.; Eskander, T.N.A.; El Hamd, M.A.; Al-Ghamdi, K.; Abu-Dief, A.M. Development of new thiazole-guanidine complexes as rapid and recoverable catalysts for the synthesis of 6-piperidin-dihydro-thia-hexaaza-s-indacene derivatives supported by DFT studies. *Appl. Organomet. Chem.* **2024**, *38*, e7454. [CrossRef]
65. El-Remaily, M.A.E.A.A.A.; Eskander, T.N.A.; Alzahrani, A.Y.A.; Alsehli, M.; Al-Ghamdi, K.; ALMughram, M.H.; El-Hady, O.M.; Feizi-Dehnayebi, M.; Abu-Dief, A.M. Tailoring of novel Ru(III) and Cr(III) Salen complexes as catalysts for a sustainable and green synthesis of dihydro-tetrazolo [1,5-a] Thiazolo [4,5-d] pyrimidin-6-yl morpholine: Experimental and theoretical approaches. *Appl. Organomet. Chem.* **2025**, *39*, e7879. [CrossRef]
66. Ismael, M.; Abdel-Mawgoud, A.M.M.; Rabia, M.K.; Abdou, A. Design and synthesis of three Fe(III) mixed-ligand complexes: Exploration of their biological and phenoxazinone synthase-like activities. *Inorganica Chim. Acta* **2020**, *505*, 119443. [CrossRef]
67. Al-Shamry, A.A.; Khalaf, M.M.; El-Lateef, H.M.A.; Yousef, T.A.; Mohamed, G.G.; El-Deen, K.M.K.; Gouda, M.; Abu-Dief, A.M. Development of new azomethine metal chelates derived from isatin: DFT and pharmaceutical studies. *Materials* **2022**, *16*, 83. [CrossRef]
68. Alkhatib, F.; Hameed, A.; Sayqal, A.; Bayazeed, A.A.; Alzahrani, S.; Al-Ahmed, Z.A.; Zaky, R.; El-Metwaly, N.M. Green-synthesis and characterization for new Schiff-base complexes; spectroscopy, conductometry, Hirshfeld properties and biological assay enhanced by in-silico study. *Arab. J. Chem.* **2020**, *13*, 6327–6340. [CrossRef]
69. Al-Farraj, E.S.; Qasem, H.A.; Aouad, M.R.; Al-Abdulkarim, H.A.; Alsaedi, W.H.; Khushaim, M.S.; Feizi-Dehnayebi, M.; Al-Ghamdi, K.; Abu-Dief, A.M. Synthesis, Structural Determination, DFT Calculation and Biological Evaluation Supported by Molecular Docking Approach of Some New Complexes Incorporating (E)-N′-(3,5-di-Tert-Butyl-2-Hydroxybenzylidene) Isonicotino Hydrazide Ligand. *Appl. Organomet. Chem.* **2025**, *39*, e7768. [CrossRef]
70. Ali, M.A.E.A.A.; Elhady, O.; Abdou, A.; Alhashmialameer, D.; Eskander, T.N.A.; Abu-Dief, A.M. Development of new 2-(Benzothiazol-2-ylimino)-2,3-dihydro-1H-imidazol-4-ol complexes as a robust catalysts for synthesis of thiazole 6-carbonitrile derivatives supported by DFT studies. *J. Mol. Struct.* **2023**, *1292*, 136188.

71. Frisch, M.; Trucks, G.; Schlegel, H.B.; Scuseria, G.E.; Robb, M.A.; Cheeseman, J.R.; Scalmani, G.; Barone, V.; Mennucci, B.; Petersson, G. *Gaussian 09, Revision D.01*; Gaussian, Inc.: Wallingford, CT, USA, 2009; 201p.
72. Mazumdar, M.; Fournier, D.; Zhu, D.W.; Cadot, C.; Poirier, D.; Lin, S.X. Binary and ternary crystal structure analyses of a novel inhibitor with 17β-HSD type 1: A lead compound for breast cancer therapy. *Biochem. J.* **2009**, *424*, 357–366. [CrossRef] [PubMed]
73. Pereira, J.H.; Goh, E.B.; Keasling, J.D.; Beller, H.R.; Adams, P.D. Structure of FabH and factors affecting the distribution of branched fatty acids in Micrococcus luteus. *Biol. Crystallogr.* **2012**, *68*, 1320–1328. [CrossRef]
74. Keniya, M.V.; Sabherwal, M.; Wilson, R.K.; Woods, M.A.; Sagatova, A.A.; Tyndall, J.D.; Monk, B.C. Crystal structures of full-length lanosterol 14α-demethylases of prominent fungal pathogens *Candida albicans* and *Candida glabrata* provide tools for antifungal discovery. *Antimicrob. Agents Chemother.* **2018**, *62*, 10–1128. [CrossRef] [PubMed]
75. Morris, G.M.; Huey, R.; Lindstrom, W.; Sanner, M.F.; Belew, R.K.; Goodsell, D.S.; Olson, A.J. AutoDock4 and AutoDockTools4: Automated docking with selective receptor flexibility. *J. Comput. Chem.* **2009**, *30*, 2785–2791. [CrossRef]
76. Feizi-Dehnayebi, M.; Ziarani, G.M.; Lohith, T.N.; Ghareghomi, S.; Panahande, Z.; Farsadrooh, M.; Majidinia, M. Probing the biological activity of isatin derivatives against human lung cancer A549 cells: Cytotoxicity, CT-DNA/BSA binding, DFT/TD-DFT, topology, ADME-Tox, docking and dynamic simulations. *J. Mol. Liq.* **2025**, *428*, 127475. [CrossRef]
77. Pettersen, E.F.; Goddard, T.D.; Huang, C.C.; Couch, G.S.; Greenblatt, D.M.; Meng, E.C.; Ferrin, T.E. UCSF Chimera—A visualization system for exploratory research and analysis. *J. Comput. Chem.* **2004**, *25*, 1605–1612. [CrossRef] [PubMed]
78. Todorova, M.; Bakalska, R.; Feizi-Dehnayebi, M.; Ziarani, G.M.; Pencheva, M.; Stojnova, K.; Milusheva, M.; Nedialkov, P.; Cherneva, E.; Kolev, T.; et al. Synthesis, Anti-Inflammatory Activity, and Docking Simulation of a Novel Styryl Quinolinium Derivative. *Appl. Sci.* **2024**, *15*, 284. [CrossRef]
79. Abdel-Rahman, L.H.; El-Khatib, R.M.; Nassr, L.A.; Abu-Dief, A.M.; Ismael, M.; Seleem, A.A. Metal based pharmacologically active agents: Synthesis, structural characterization, molecular modeling, CT-DNA binding studies and in vitro antimicrobial screening of iron (II) bromosalicylidene amino acid chelates. *Spectrochim. Acta Part A Mol. Biomol. Spectrosc.* **2014**, *117*, 366–378. [CrossRef]
80. Abu-Dief, A.M.; Nassr, L.A. Tailoring, physicochemical characterization, antibacterial and DNA binding mode studies of Cu(II) Schiff bases amino acid bioactive agents incorporating 5-bromo-2-hydroxybenzaldehyde. *J. Iran. Chem. Soc.* **2015**, *12*, 943–955. [CrossRef]
81. Abdel-Rahman, L.H.; Abu-Dief, A.M.; El-Khatib, R.M.; Abdel-Fatah, S.M. Sonochemical synthesis, DNA binding, antimicrobial evaluation and in vitro anticancer activity of three new nano-sized Cu(II), Co(II) and Ni(II) chelates based on tri-dentate NOO imine ligands as precursors for metal oxides. *J. Photochem. Photobiol. B Biol.* **2016**, *162*, 298–308. [CrossRef]
82. Abdel-Rahman, L.H.; Abu-Dief, A.M.; Newair, E.F.; Hamdan, S.K. Some new nano-sized Cr(III), Fe(II), Co(II), and Ni(II) complexes incorporating 2-((E)-(pyridine-2-ylimino) methyl) napthalen-1-ol ligand: Structural characterization, electrochemical, antioxidant, antimicrobial, antiviral assessment and DNA interaction. *J. Photochem. Photobiol. B Biol.* **2016**, *160*, 18–31. [CrossRef]
83. Abdel-Rahman, L.H.; Ismail, N.M.; Ismael, M.; Abu-Dief, A.M.; Ahmed, E.A.H. Synthesis, characterization, DFT calculations and biological studies of Mn(II), Fe(II), Co(II) and Cd(II) complexes based on a tetradentate ONNO donor Schiff base ligand. *J. Mol. Struct.* **2017**, *1134*, 851–862. [CrossRef]
84. Abu-Dief, A.M.; Nassar, I.F.; Elsayed, W.H. Magnetic $NiFe_2O_4$ nanoparticles: Efficient, heterogeneous and reusable catalyst for synthesis of acetylferrocene chalcones and their anti-tumour activity. *Appl. Organomet. Chem.* **2016**, *30*, 917–923. [CrossRef]
85. Ferrari, E.; Asti, M.; Benassi, R.; Pignedoli, F.; Saladini, M. Metal binding ability of curcumin derivatives: A theoretical vs. experimental approach. *Dalton Trans.* **2013**, *42*, 5304–5313. [CrossRef] [PubMed]

Disclaimer/Publisher's Note: The statements, opinions and data contained in all publications are solely those of the individual author(s) and contributor(s) and not of MDPI and/or the editor(s). MDPI and/or the editor(s) disclaim responsibility for any injury to people or property resulting from any ideas, methods, instructions or products referred to in the content.